

,

“ ” _____ 2023 .

()

« »

: « , »

: _____ .

: _____ .

: _____ .

MINISTRY OF EDUCATION AND SCIENCE OF UKRAINE
NATIONAL AVIATION UNIVERSITY
Faculty of Air Navigation, Electronics and Telecommunications
Aerospace Control Systems Department

ACCEPT TO PROTECTION

Head of the ACS Department

_____ Yuri MELNYK

“_____” _____ 2023 y.

QUALIFICATION PAPER

(EXPLANATORY NOTE)

FOR THE ACADEMIC DEGREE OF BACHELOR

Subject: «The bias correction in a vibratory gyroscope operating in the rate-integrating mode»

Performer: _____ Starozhytnyk D.M.

Supervised: _____ Chikovani V.V.

Norm control: _____ Chikovani V.V.

Kyiv 2023

: 151 "

“ _____ ” _____ 2023 .

1.

:«

».

«13» 2023 . No 507/

2.

: 10.03.23 10.06.23

3.

:

10 / ,

$Q=3\times 10^4$,

$\Delta Q 10^3$,

$f_r=4\times 10^3$,

$\Delta f=0.03$.

4.

:

1.

;

2:

MEMS ,

;

3:

5. , :
Power Point.

6. -

| | | | |
|----|--|-------------------------|--|
| . | | | |
| 1. | | 10.05.2023 – 11.05.2023 | |
| 2. | | 12.05.2023 – 13.05.2023 | |
| 3. | | 14.05.2023 – 19.05.2023 | |
| 4. | | 20.05.2023 – 25.05.2023 | |
| 5. | | 30.05.2023 – 05.06.2023 | |
| 6. | | 08.06.2023 – 11.06.2023 | |

7. : “10” 2023 .

(signature)

(signature)

NATIONAL AVIATION UNIVERSITY

Faculty of Air Navigation, Electronics and Telecommunications

Aerospace Control Systems Department

Specialty: 151 "Automation and computer-integrated technologies"

APPROVED

Head of Department

Melnyk Yu.V.

" ____ " _____ 2023

Qualification Paper Assignment for Graduate Student

Starozhytnyk Dmytro Mykhailovych

- 1. The qualification paper title** «The bias correction in a vibratory gyroscope operating in the rate-integrating mode» was approved by Rector's order of «13» April 2023 No 507/
- 2. The paper to be completed between:** 10.03.23 and 10.06.23
- 3. Initial data for the paper:** The vibrating gyroscope in the rate-integrating mode has an insensitivity zone of 10 deg/s, the resonator Q-factor is $Q=3\times 10^4$, the Q-factor mismatch is $\Delta Q = 10^3$, the resonant frequency is $f_r = 4\times 10^3$ Hz, the frequency mismatch is $\Delta f = 0.03$ Hz.
- 4. The content of the explanatory note:**
Section 1. Overview of the vibratory gyroscope modes of operation; Section 2. The rate-integrating MEMS vibratory gyroscopes; Section 3. The periodic bias model and its correction.
- 5. The list of mandatory illustrations:**
Graphs of simulation and calculation results. Presentation materials in Power Point

6. Timetable:

| | Assignment | Dates of completion | Completion mark |
|----|--|-------------------------|-----------------|
| 1. | Task | 10.05.2023 – 11.05.2023 | |
| 2. | Purpose formation and describing the main research tasks | 12.05.2023 – 13.05.2023 | |
| 3. | Analysis of existing methods | 14.05.2023 – 19.05.2023 | |
| 4. | Analysis of existing systems | 20.05.2023 – 25.05.2023 | |
| 5. | Development of software for error correction of MEMS gyroscope | 30.05.2023 – 05.06.2023 | |
| 6. | Preparation of presentation and handouts | 08.06.2023 – 11.06.2023 | |

7. Date of task receiving: “10” May 2023 y.

Diploma thesis supervisor

(signature)

Chilovani V.V.

Issued task accepted

(signature)

Starozhytnyk D.M.

: 90 ., 38 ., 1 ., 76

.

,

—

—

—

,

.

—

Matlab.

,

.

,

.

.

ABSTRACT

Text part of the work: 90 p., 38 fig., 1 table, 76 references.

Object of research - Vibration gyroscope of low quality

Purpose of the work - Model of errors of the periodic drift component of the vibration gyroscope

Subject of the research - To improve the vibration gyroscope operating in the mode of angular velocity integration by correcting its errors.

Methods of research - Theoretical analysis and experimental studies using modeling in Matlab.

In this work, we investigated the operation of a vibration gyroscope in the mode of angular velocity integration, that is, the gyroscope measures the full angle of rotation relative to inertial space. The measurement accuracy is determined mainly by the periodic drift of the gyroscope caused by the manufacturing errors of the resonator. In this work, experimental studies of the measurement of the angle of rotation are carried out and a model for correcting the periodic error is built, and the increase in the accuracy of measuring the full angle of rotation is shown.

CONTENT

| | |
|--|----|
| Introduction | 10 |
| Problem statement | 12 |
| SECTION 1. OVERVIEW OF THE VIBRATORY GYROSCOPE MODES OF OPERATION | 13 |
| 1.1 Basic Architecture | 13 |
| 1.2 Drive-Mode Operation | 15 |
| 1.3 Sense-Mode Operation | 16 |
| 1.4 Designs of the MEMS gyroscopes its designs, application, characteristics and parameters | 17 |
| 1.4.1 Gimbal Gyroscopes | 17 |
| 1.4.2 Tuning Fork Gyroscopes | 22 |
| 1.4.3 Vibrating Ring Gyroscopes | 27 |
| 1.4.4 Multi-Axis Gyroscopes | 37 |
| SECTION 2. THE RATE-INTEGRATING MEMS VIBRATORY GYROSCOPES | 42 |
| 2.1 Principle of operation of the rate-integrating MEMS vibratory gyroscopes | 42 |
| 2.2 Rate Mode Principle of Operation | 44 |
| 2.3 Rate-integrating mode principle of operation | 48 |
| 2.4 Two-dimensional pendulum model | 50 |
| SECTION 3. THE PERIODIC BIAS MODEL AND ITS CORRECTION | 56 |
| 3.1. Dynamic equation of a resonator oscillation in slow variables | 56 |
| 3.2. The angle error determination, approximation and correction | 58 |
| Conclusion | 65 |
| References | 66 |
| Appendix | 76 |

Introduction

The gyroscope is an inertial sensor that is used for the measurement or control of the orientation and rotational velocity of a body. In the early 17th century, people occasionally used spinning mass objects for navigation purposes. The spinning mass gyroscope concept was first developed by French scientist Jean Bernard Leon Foucault in 1852 [1]. In the late 18th century, the usage of the gyroscope was extended to ship navigation at sea. At the beginning of the 20th century, the traditional spinning mass gyroscope started to be used in aircraft [2]. In the 1960s, the concept of optical lasers for gyroscopes was introduced, which provided higher precision and better sensitivity and brought a tremendous leap forward for aerospace and military applications [3]. However, the costs associated with optical gyroscopes were quite high, and this provided motivation for the development of micro-electromechanical systems (MEMS) vibrating gyroscopes. Over the past few decades, a large number of MEMS gyroscopic technologies have been developed with high sensitivity, high scale factor, and reduced fabrication costs [4].

Nowadays, in our daily life routine, smart devices are commonly used for tracking and their navigation capability requires global positioning systems, such as mobile phones, smartwatches, and vehicles. The navigation systems comprise inertial measurement units (IMU) [5], which are installed in the smart electronic devices [6]. The IMU typically consists of multiple inertial sensors, including a gyroscope, accelerometer, and magnetometers. All of these sensors work from different scientific principles: the gyroscope is a rotational motion inertial sensor that detects the change of position when rotation occurs, the accelerometer is a translational motion sensor that detects linear acceleration [7], and the magnetometer gives guidance in the coordinate system [8].

The usage of the MEMS gyroscope has increased enormously over the last 20 years. These sensors have been extensively used in smart devices, automotive industries, household applications, aerospace, military applications, and so on [9,10]. The research

on the MEMS vibratory gyroscopes started gaining maturity and moved towards practical designs at the start of the 21st century. In the early stages, only a few research groups tended to research in this area. However, at the beginning of the 2000s, more research groups showed interest and developed a variety of designs for MEMS vibrating gyroscopes [11]. The gyroscope's sensitivity and performance degrade when it is exposed to an unwanted atmosphere. Some of the prominent issues that deteriorate the stability and reliability of MEMS for gyroscopes range from microfabrication process stability (beam stiffness, material properties, and critical dimension losses) to exposure to harsh environments (space, elevated temperature, radiation) and external vibrations.

Problem statement

A Vibratory gyroscope overview is presented in this work. The operation principle of the rate and rate-integrating (or whole angle) modes, with a focus on the rate-integrating mode, are presented. The rate-integrating vibratory gyroscope periodic error is considered and shown graphically in a simple example under the real gyro's constant angle rate rotation. To build the periodic error mathematical model, an approximation of the real gyro's error is fulfilled. After correction, the residual error is graphically presented. The gyro accuracy increase is calculated by the results of the correction of the periodic error.

SECTION 1. OVERVIEW OF THE VIBRATORY GYROSCOPE MODES OF OPERATION

The basic principle of operation of a MEMS vibration gyroscope consists of two vibration operating modes: one is the drive mode, which provides is constantly changing along the drive axis, and the other is the detection method, which detects the movement of vibration along the sensing axis when external rotation is provided.

1.1 Basic Architecture

Most MEMS vibration gyroscopes have proof masses "m" with two orthogonal degrees of freedom, vertical and horizontal. When the gyroscope is oscillating continuously at the resonant frequency in one direction, oscillations in the orthogonal direction remain absent until an external rotation occurs in the gyroscope. When the external rotation occurs, this rotation causes a shift in the energy of the first oscillation in the orthogonal direction due to the Coriolis effect [12]. The basic schematic diagram of an oscillatory system with two degrees of mass freedom is shown in Figure 1.1.

| | | | | | | | |
|-----------------------|-----------------------|--|--|---|----------------|--------------|--------------|
| <i>ACS Department</i> | | | | <i>Name</i> | | | |
| <i>Performed.</i> | <i>D.Starozhytnyk</i> | | | <i>Overview Of The Vibratory Gyroscope Modes Of Operation</i> | <i>N..</i> | <i>Page.</i> | <i>Pages</i> |
| <i>Supervisor</i> | <i>V. Chikovani</i> | | | | | 13 | 27 |
| <i>Consultant</i> | <i>V. Chikovani</i> | | | | 402 151 | | |
| <i>S. controller.</i> | <i>V. Chikovani</i> | | | | | | |
| <i>Dep. head</i> | <i>Yu. Melnyk</i> | | | | | | |

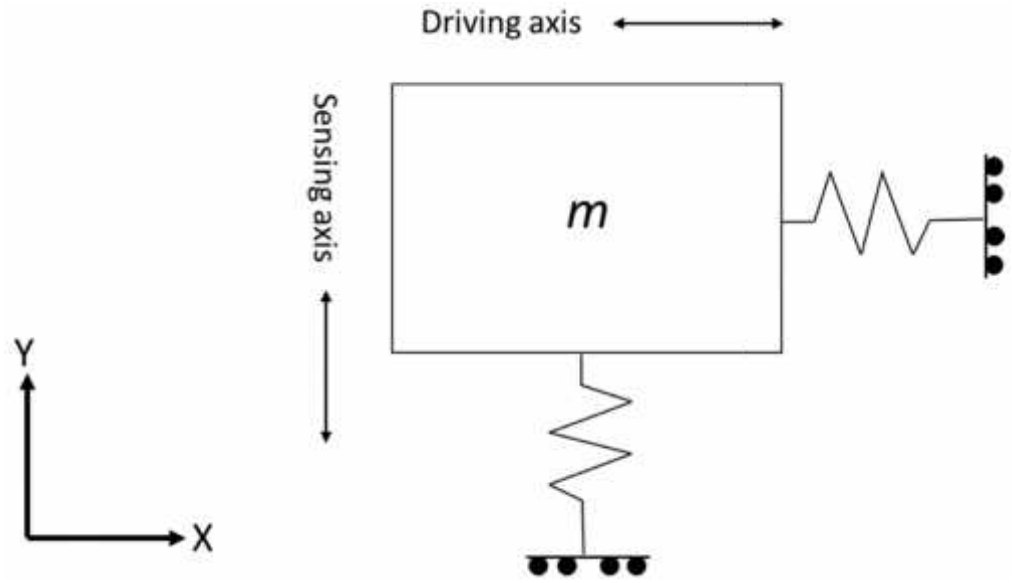


Figure 1.1 - Simple depiction of a proof mass vibrating system.

The simplest two degrees of freedom equations of motion for MEMS vibrating gyroscopes and the equation of the Coriolis force are given below.

$$m \frac{d^2x}{dt^2} + c \frac{dx}{dt} + kx = F_D + 2m\Omega \frac{dy}{dt}, \quad (1.1)$$

The sensing mode response is typically very small in magnitude compared to the control mode response, so the Coriolis force $2m\Omega \frac{dy}{dt}$ will become negligible, and Equation (1.1) can be written as below.

$$m \frac{d^2x}{dt^2} + c \frac{dx}{dt} + kx = F_D, \quad (1.2)$$

$$m \frac{d^2y}{dt^2} + c \frac{dy}{dt} + ky = F_S - F_C, \quad (1.3)$$

$$F_C = -2m\Omega \frac{dx}{dt}, \quad (1.4)$$

where F_D , F_S , and F_C are the driving, sensing, and Coriolis forces, respectively, m is the inertial mass, x is the displacement of the driving motion, y is the displacement of the sensing motion, c is the damping coefficient, k is the stiffness constant, and Ω is the external rotation rate.

The simplest structure of a vibrating MEMS gyroscope is shown in Figure 1.2: the proof mass, driving and sensing electrodes, and a system of suspension beams with four fixed support posts are placed above the substrate [13]. The driving system consists of driving electrodes that provide oscillations with a certain amplitude, and the sensing system, which consists of a Coriolis force detector. The proof mass becomes an oscillator when the driving electrodes provide a constant and continuous pulse along the direction of the driving axis. The same proof mass changes its oscillatory motion to an orthogonal direction to the axis of rotation when it is externally rotated. Sensing electrodes on the orthogonal axis detect the Coriolis force, which is created by a mixture of the driving impulse and external rotation.

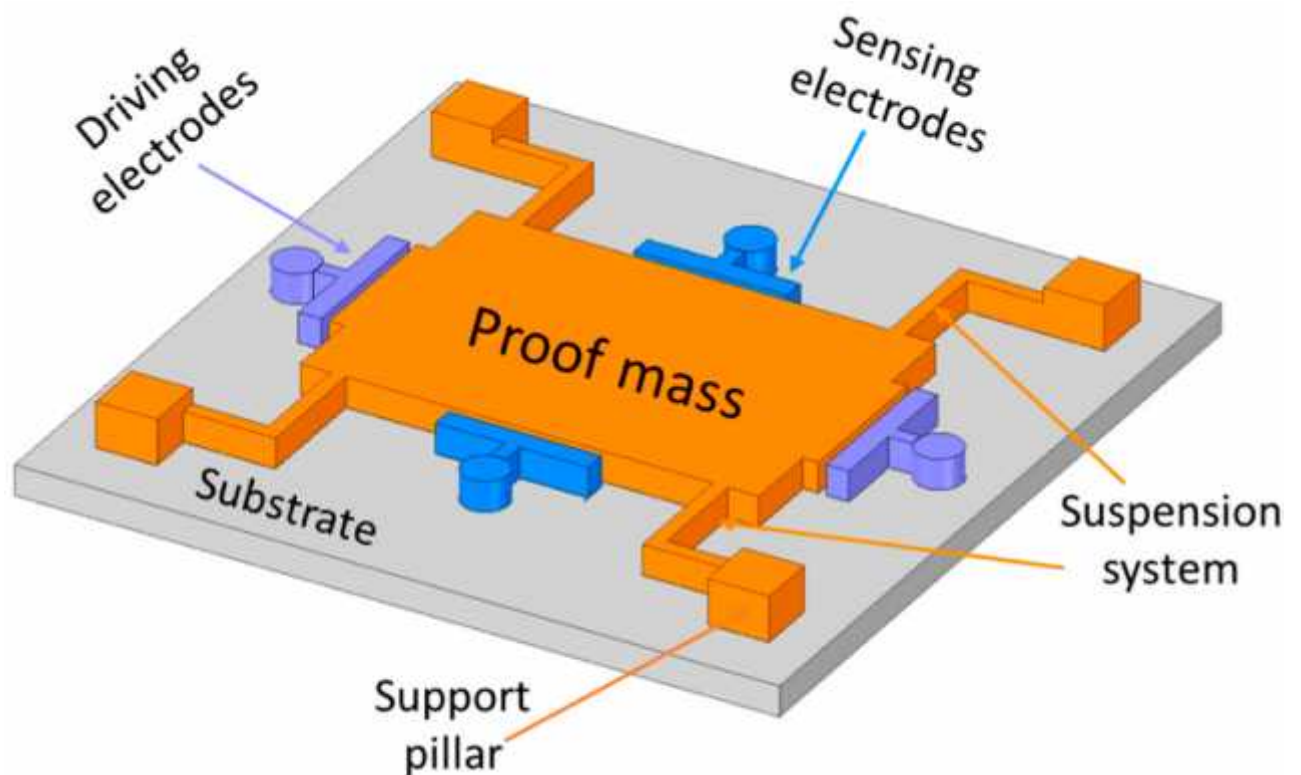


Figure 1.2 - Schematic architecture of a single proof mass vibrating gyroscope.

1.2 Drive-Mode Operation

Many of the MEMS vibrating gyroscopes comprise the combination of proof masses with a spring system to form a single-degree-of-freedom resonator circuit, as shown in Figure 1.3.

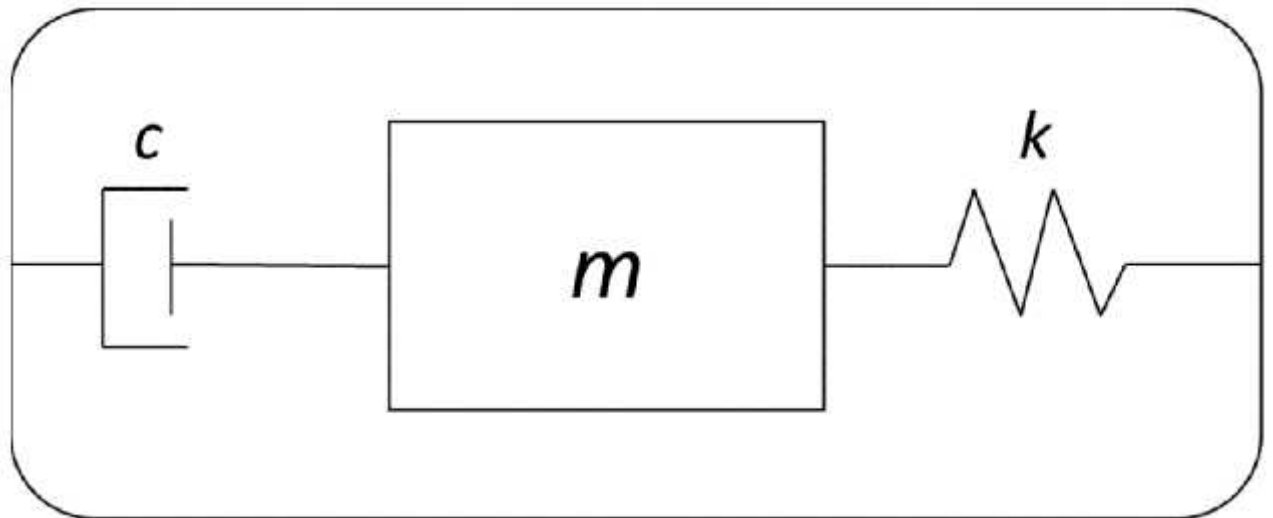


Figure 1.3 - Typical one degree of freedom resonator

The equation of motion for single-degree-of-freedom is given below. Here, “ m ” is the proof mass, “ c ” is the damping constant, and “ k ” is the stiffness constant.

$$m \frac{d^2x}{dt^2} + c \frac{dx}{dt} + kx = F \quad (1.5)$$

1.3 Sense-Mode Operation

The operation of the sensor mode depends on the Coriolis effect. The Coriolis force F_C requires operation in a drive-mode which leads to continuous oscillations of the proof mass at a given resonant frequency using drive electrodes along the drive axis. When the gyroscope is subjected to rotation, the developed Coriolis force excites the sensitive mode system, as shown in equation (1.4).

Consider that the sensing-mode system also has one degree of freedom resonator, similar to the driving-mode system. To understand the Coriolis force, assume that the driving mode system oscillates at the driving resonant frequency with a stable driving amplitude x_0 . The drive motion amplitude is given as $x = x_0 \sin(\omega_D t + \phi_D)$. The Coriolis force equation becomes:

$$F_C = -2m_C \Omega x_0 \omega_D \cos(\omega_D t + \phi_D) \quad (1.6)$$

1.4 Designs of the MEMS gyroscopes its designs, application, characteristics and parameters

In the evolution of integrated circuit (IC) technology, the miniaturization of microelectromechanical system sensors has played a significant role in reducing the size of devices. The demand for MEMS vibration gyroscopes for sensor applications has increased significantly due to their small and compact size, energy efficiency, overall low manufacturing cost, high performance and sensitivity, and mass production [14]. Exhaustive research has been conducted on many types of gyroscopes such as dual-axis, multi-axis, single-axis, single mass, dual mass, and decoupled gyroscopes. The MEMS gyroscope works on different mechanisms. The most common are the electrostatic [15,16] and piezoelectric [17,18] mechanisms, compared to the electromagnetic [19] and electrothermal [20] mechanisms. In recent developments, some key gyroscope designs, such as the vibrating ring, tuning fork, decoupled, and dual masses [21], have emerged as the most popular gyroscope structures [22]. In this section, four main types of MEMS-based vibration gyroscopes are discussed.

1.4.1 Gimbal Gyroscopes

The term "MEMS gimbal gyroscope" is derived from a traditional gimbal gyroscope with a spinning rotor, where the spinning rotor is mounted on two freely spaced gimbal systems: an inner and an outer gimbal. Previously, a dynamic attitude gyroscope and a control torque gyroscope were used for military purposes to track and measure satellite motion [23]. However, in the late 1980s, the Draper Laboratory began research on the use of vibrating elements for gyroscopic purposes. The first micromachined gyroscope was developed by the Draper laboratory in 1988 [24]. Bockenhorn et al. demonstrated the first new micromechanically driven gyroscope

that did not have a rotating part. The gyroscope design was based on two gimbal systems: one was external and the other was internal. A vertical bar was mounted on the internal gimbal. The inner gimbal was the sensing element, while the outer gimbal was attached to the motor. The two gimbals were connected using orthogonal bending joints; the outer gimbal was used to vibrate at a predetermined frequency, making the inner gimbal sensitive enough to detect rotational motion with any external rotation. In addition, they fabricated a silicon monolithic micromechanical gyroscope. All the structural elements were made on a single substrate, which was the beginning of mass production of this small-sized vibration gyroscope. The dimensions of the gimbal structure were $350\ \mu\text{m} \times 500\ \mu\text{m}$. The outer gimbal was driven electrostatically by electrodes with a predetermined amplitude. This motion was transmitted to the inner gimbal, causing the inertial element to oscillate. When rotation was applied to the gyroscope, the Coriolis force shifted the oscillations of the internal gimbal toward the weak axis with equal amplitude to the rotation frequency. The output motion of the internal gimbal was sensed capacitively using sensitive electrodes placed near the gimbal structure. The schematic diagram of the micromechanical gimbal gyroscope is shown in Figure 1.4 [25].

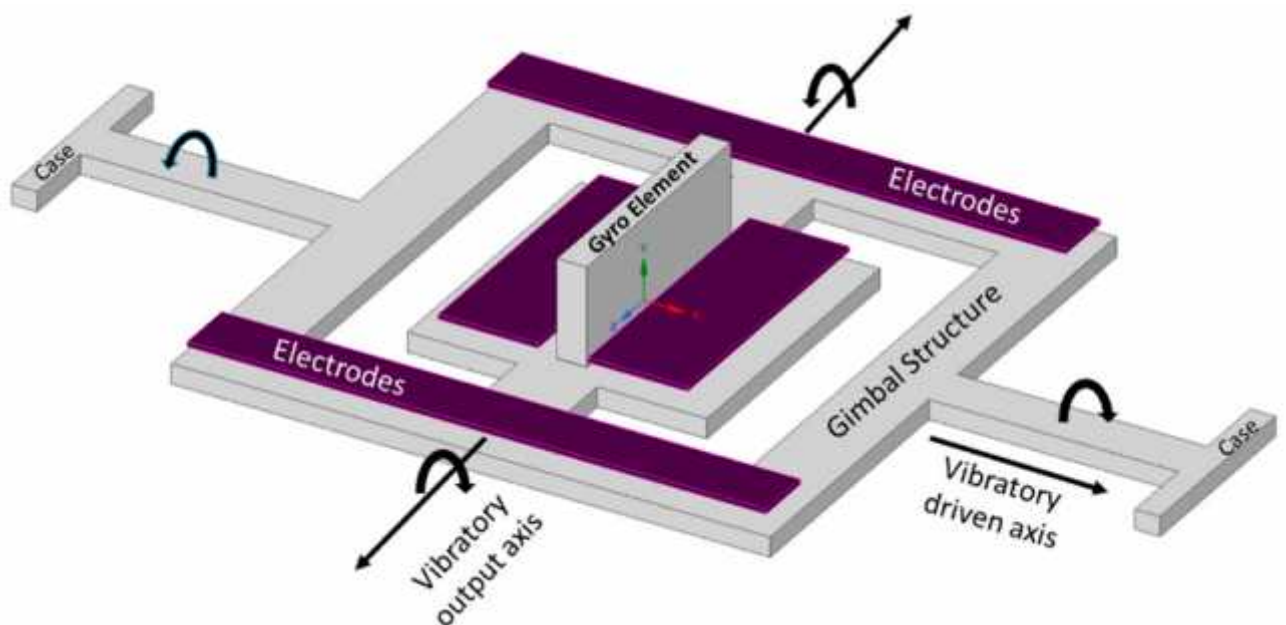


Figure 1.4 - Schematic diagram of Draper laboratory's micromachined gimbal gyroscope

In 1996, Draper's laboratory developed the third stage of the design of the Vibrating Wheel on a Gimbal Gyroscope (VWOG). The concept featured a vibrating wheel, approximately 1 mm in diameter, at a predetermined resonance. The entire structure was suspended on a Pyrex substrate. The outer ring of the wheel structure was considered the proof mass, and fixed stator combs and a number of wheel-attached combs were attached to the substrate. The wheel structure had four beams suspended above the substrate and was centrally fixed to the substrate. The wheel structure was surrounded by electrodes, and these electrodes were used to excite the wheel ring. During operation, the wheel vibrated in a sinusoidal pattern, applying a control voltage to the stationary stator combs. When the rotation was applied to the gyroscope, the Coriolis force shifted the driving motion to the output axis. This motion was recorded by capacitor plates placed under the wheel structure and on a Pyrex substrate. The design showed excellent promise in terms of sensitivity, and the sensitivity was better than 0.1 deg/s in the 60 Hz frequency band [26] compared to the Draper Laboratory's tuning fork gyroscope [27].

Geiger et al. demonstrated a new high-performance, low-cost, micro-machine gyroscope with a rotational frequency [28]. The concept of this gyroscope was to combine a double gimbal and a comb structure gyro for primary and secondary oscillations. The gyroscope showed promising proof results, as the angular random walk (ARW) was measured at 0.14 deg/h and the shear stability was recorded at 65 deg/h. The structure of the device consisted of comb drives, four fixed comb electrodes, a secondary oscillator, and detector electrodes placed above the substrate. The comb actuators were used to provide rotational motion along the z-axis using electrostatic actuation. The other fixed comb electrodes perceived the primary rotational motion. The Coriolis force was generated by the rotation of the device along the x-axis. The Coriolis force was used to create another rotational motion

along the y-axis; therefore, the secondary structure of the oscillator moved with the Coriolis force. The motion was sensed capacitively using detector electrodes placed over the substrate.

The diaphragm gyroscope was designed with two gimbal structures, an inner and an outer gimbal, and could operate at atmospheric pressure [29]. Both the inner and outer gimbals were aligned with the inner and outer coils, respectively. The entire gimbal structure was supported by torsion bars that were placed perpendicular to the gimbal structure. The conductive inner coils caused the inner gimbal to oscillate at a predetermined resonant frequency around the torsion bars. The outer gimbal was in a stationary state because the oscillations of the inner gimbal were parallel to the torsion bars of the outer gimbal. The Coriolis force occurred at the center of masses when the angular velocity was applied perpendicularly. The Coriolis force was used to initiate the oscillations of the outer gimbal; subsequently, the outer coils provided the electromotive force for voltage detection.

Two MEMS gyroscope gimbal structures containing Ni-Fe alloy were fabricated using the UV-LIGA process based on SU-8 [30]. The authors claim that this process overcame the disadvantages of the micromachining process. First, an 8 μm thick nickel layer was applied as a structural layer. However, the nickel material is prone to residual stresses, and these stresses caused the structural layer to deflect and touch the electrode, which was placed under the device structure. This structural layer deflection problem caused the device to shorten as it touched the lower electrodes. To solve this problem, a Ni-Fe alloy based on 70% Ni, 15% Fe, and 10% C was used to avoid deflection of the structural layer. The schematic diagram of the Ni-Fe gimbal MEMS gyroscope is shown in Figure 1.5.

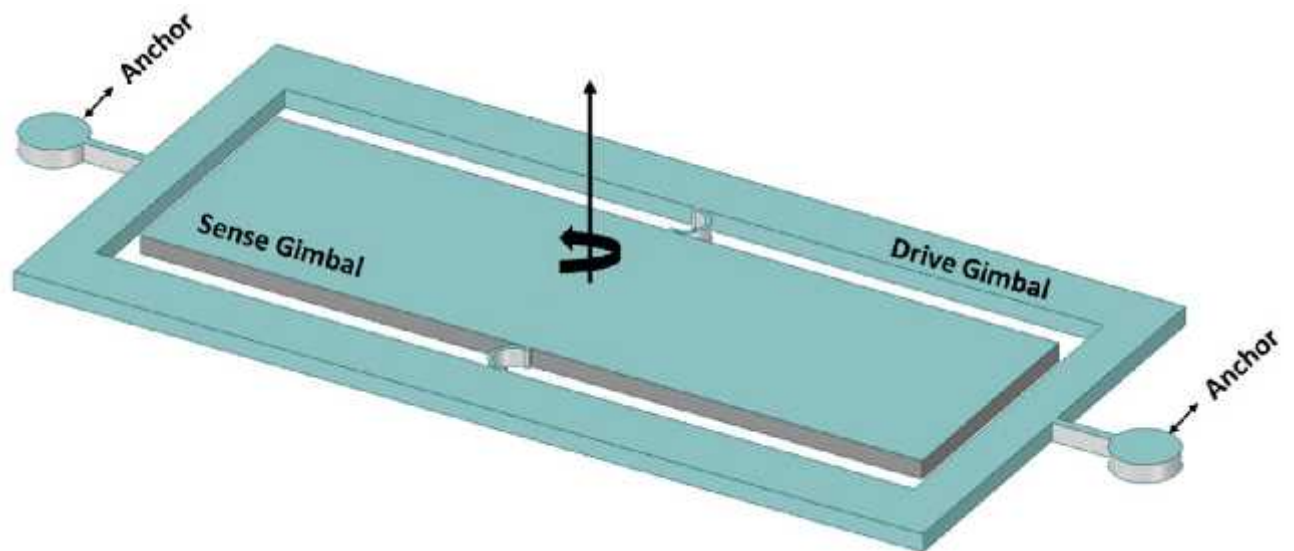


Figure 1.5- Ni–Fe alloy-based two-gimbal system gyroscope.

Lee et al. investigated the scale factor and linearity error using different shapes and masses for gimbal gyros [31]. In this study, a different number of shapes and masses were considered, and the designs are shown in Figure 1.6. The scale factor and linearity error were obtained by varying the capacitance with different gimbal shapes. The different designs showed different results; for example, the round shape design provides a high scale factor compared to the others. However, the round shape did not provide a good linearity error. The hexagonal shape structure has the lowest linearity error and acceptable scale factor, making it a more realistic and stable design for MEMS gimbal gyros.

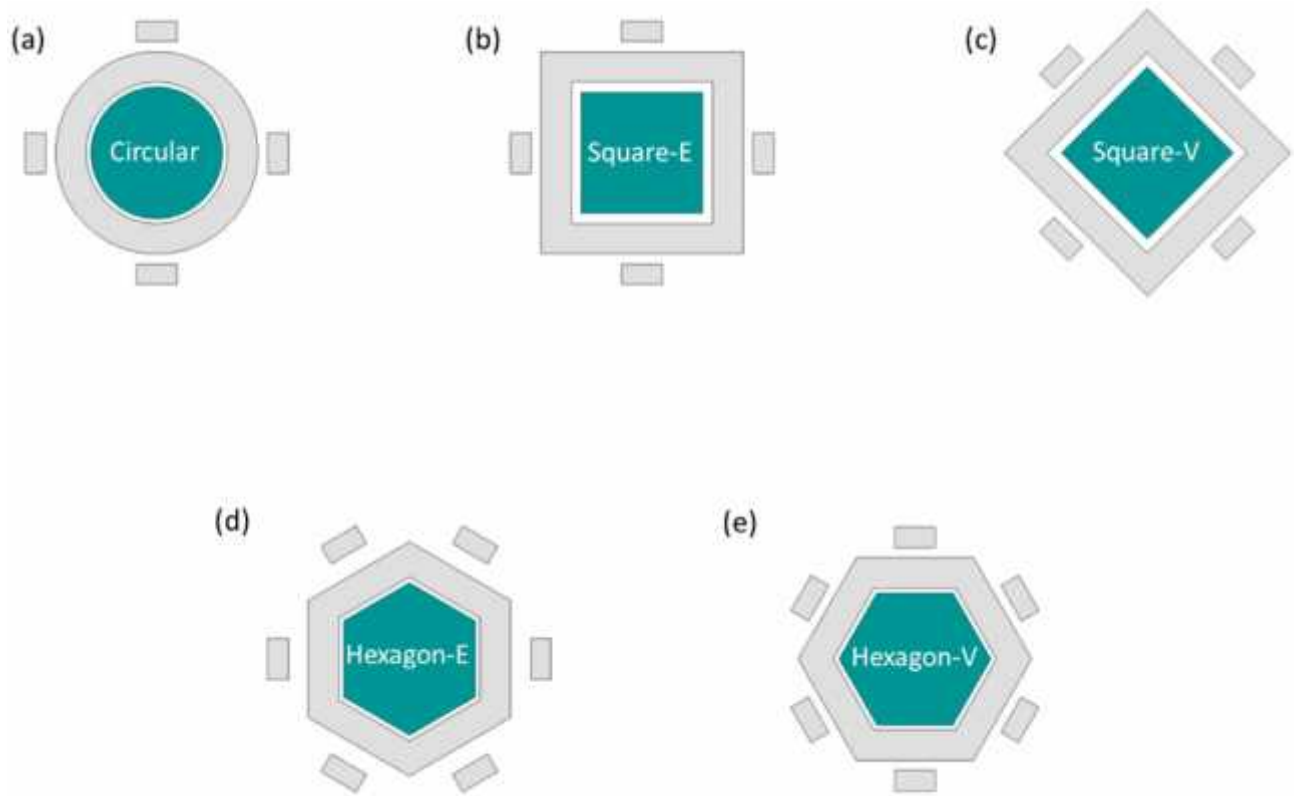


Figure 1.6 - Study of different shapes of an MEMS vibrating wheel on a gimbal gyroscope. (a) circular (b) square-edge (c) square-vertex (d) hexagon-edge (e) hexagon-vertex.

1.4.2 Tuning Fork Gyroscopes

Tuning fork gyroscopes are one of the most popular designs of MEMS gyroscopes. These designs have two identical masses moving with the same amplitude but in opposite directions [32]. When a rotational motion perpendicular to the driving axis occurs, this motion creates a Coriolis force that shifts the driving motion toward the sensing axis. The driving mechanism and the sensing mechanism, which uses electrostatic actuation and capacitive sensing, respectively, provide an increased level of sensitivity compared to other designs [33]. A schematic illustration of the operation of a gyroscope with a MEMS tuning fork is shown in Figure 1.7.

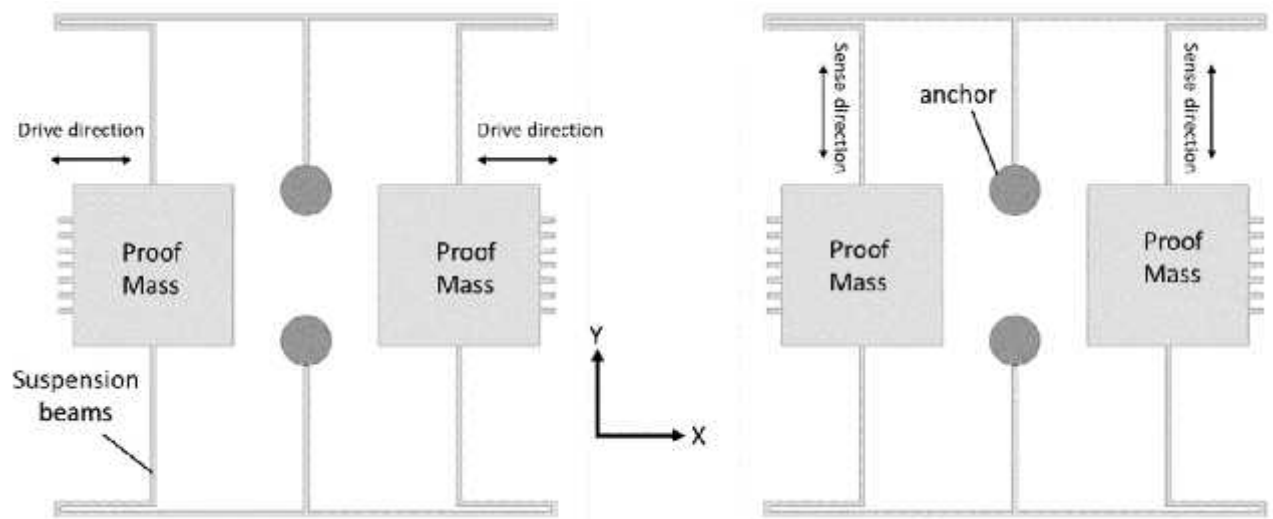


Figure 1.7 - Working operation of a basic MEMS tuning fork gyroscope

In 1993, the first micromechanical tuning fork gyroscope was developed using nickel electroforming technology, reactive ion etching of polysilicon, and single crystal silicon on glass technology. The gyroscope was 1 mm in size, and the goal was to achieve a bias stability of less than 100 deg/h. Initially, all three manufacturing technologies were considered, but in the end, only one was chosen because it showed good results. The nickel electroforming technology made it possible to reduce the size of the elements to 6 microns, but it was abandoned due to the poor quality and possible fatigue associated with the nickel material. Silicon-on-glass fabrication provided very low stray capacitance, but it was limited by symmetrical bonding wires. Reactive ion etching with polysilicon material provided excellent properties such as low corrosion rate and good heat resistance, and so it was chosen as the fabrication technology. The tuning fork gyroscope had two proof masses with perforations; both masses rotated at a given resonant frequency, but in opposite directions. When the gyroscope rotates, one proof mass rises up and the other falls down. Sensitive electrodes placed under the proof masses capacitively sensed the change in displacement. A scale factor of 90 mV/deg/s was achieved. The resolution was 0.1 deg/s, and the displacement stability was 0.2 deg/s in a 1 Hz bandwidth.

Che et al. fabricated a novel tuning fork gyroscope using silicon interconnect and deep reactive ion etching (DRIE) technology [34]. The gyroscope had two symmetrical proof masses with several driving and sensing bars. The entire structure was supported by four anchors connected to spring beams placed on a glass substrate. The gyroscope operated electrostatically, and the rotational motion was recorded capacitively at atmospheric pressure. The gyroscope was tested, and a significant mode mismatch of 0.12 kHz was found between the drive and readout modes. The operating frequency was about 2.87 kHz, the sensing frequency was 2.99 kHz, and the Q factor was 804 and 789 for the operating and sensing frequencies, respectively.

A high-resolution gyroscope based on a single-crystal silicon MEMS with a tuning fork insulator was demonstrated in [35]. The gyroscope had two proof masses that were driven electrostatically by moving electrodes at a given resonant frequency along the x-axis. The Coriolis force was induced when the device experienced rotational motion around the z-axis, and this rotation was sensed capacitively by sensing electrodes along the y-axis. A schematic view of the high-quality MEMS tuning fork gyroscope is shown in Figure 8. This design allowed for a Q factor of 81.000 for the motion mode and 64.000 for the sensing mode. The gyroscope structure was fabricated on a 40 μm silicon single crystal on an insulating substrate. The simplest two-wafer process was used to fabricate the gyroscope. The structural layer of moving objects and comb electrodes were first removed from the back side of the wafer by etching the silicon layer using the Bosch process. Reactive ion etching was used to remove the buried oxide layer, leaving a patterned layer that carried the suspended structure. The high resolution of the gyroscope was achieved by electrostatically balancing the control and sensing modes through electrode tuning and achieving high quality coefficients with a sensitivity of 1.25 mV/deg/s.

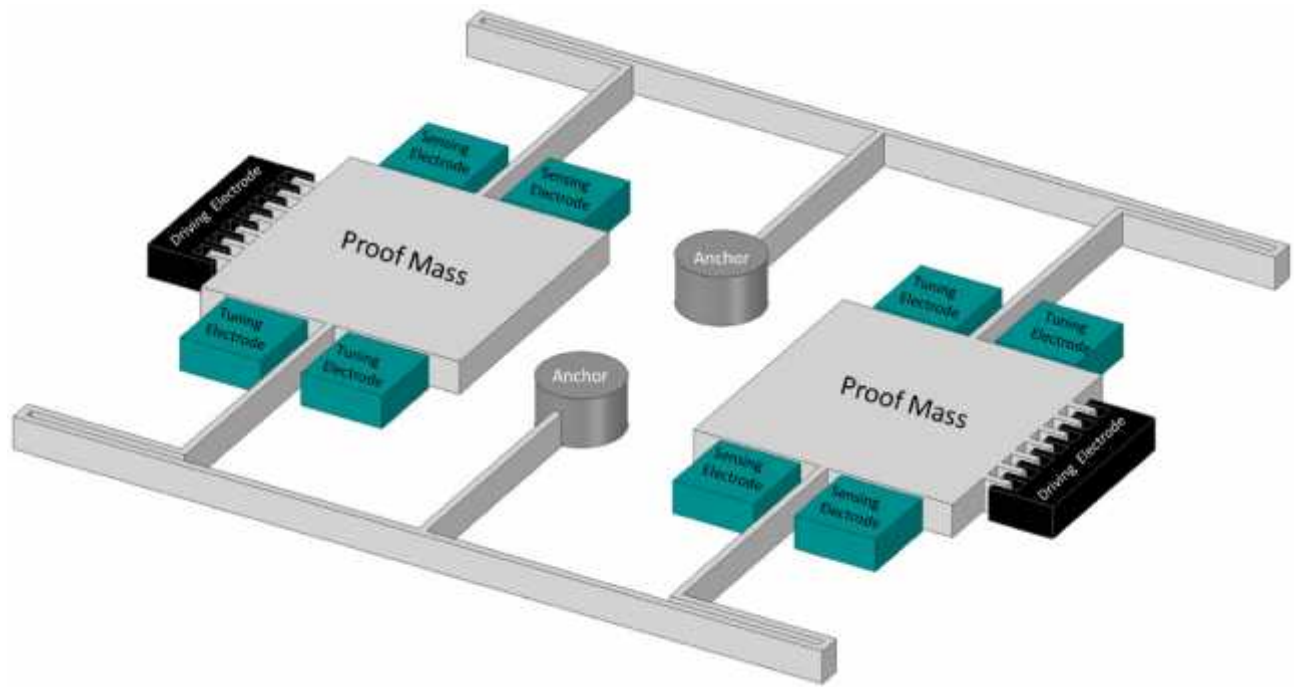


Figure 1.8 - Schematic diagram of high Q MEMS tuning fork gyroscope.

A gyroscope with a forked tuning fork in the z-axis, which had a free-standing structure with low damping in the air, was developed by Nguyen et al. [36]. Various factors were considered to improve the overall performance of the gyroscope, such as eliminating the damping of the compressive film by designing the driving and sensing structure to oscillate in-plane and removing the substrate under the gyroscope structure to negate the air damping of the side film. The proposed gyroscope is shown in Figure 1.9. The simulated control and sensing frequencies were 9.78 kHz and 9.76 kHz, respectively. The Q factor was measured at 111.2, and the sensitivity of the gyroscope under atmospheric conditions was 11.56 mV/deg/s.

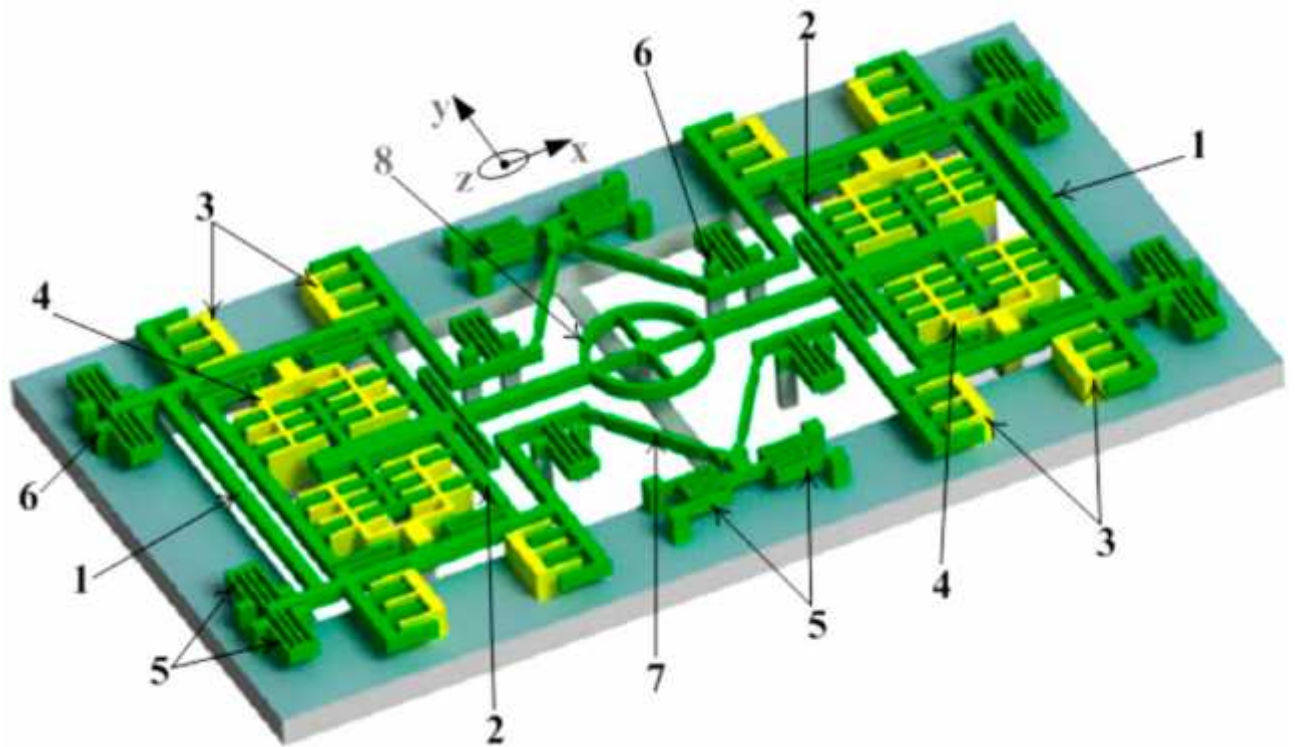


Figure 1.9 - Schematic representation of the z-axis freestanding gyroscope [43]: 1— External frame, 2—internal frame, 3—drive electrodes, 4—sense electrode, 5— spring beams, 6—support anchors, 7—linear beams, and 8—circular rotating ring.

Guan et al. [37] presented an article on a new tuning fork gyroscope based on MEMS with anchor connection. The new design helped to analyze the order of the vibration mode and gyroscopic sensitivity. The tuning fork gyroscope used a lever system for the drive mode frequency and a fixed four-beam coupling spring for the sensing mode frequency. The simulated sensing frequencies recorded for the in-phase and out-of-phase modes were 4006 kHz and 4464 kHz, respectively. However, the in-phase frequency with anchor connection was 5958 kHz, which is almost 50% higher than the simulated in-phase sensing frequency. The same researchers continued their work [38] and proposed a new design of the MEMS tuning fork gyroscope with the diamond anchor coupling method, which is shown in Figure 1.10.

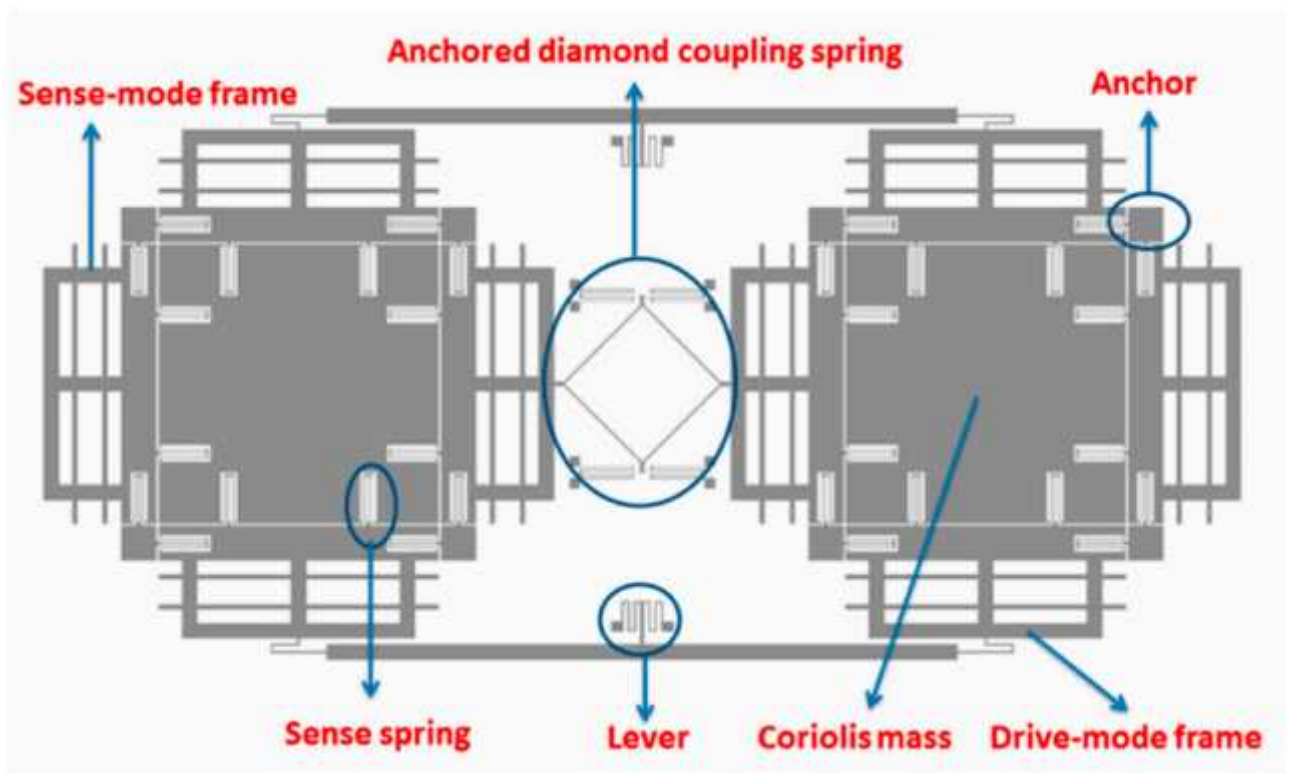


Figure 1.10 - Schematic view of tuning fork gyroscope with anchored diamond coupling method [45].

Trusov et al. reported a high-quality tuning fork gyroscope with a rate integration method, and the gyroscope demonstrated a quality factor for the control and sensing modes of 310 k and 640 k, respectively [39].

1.4.3 Vibrating Ring Gyroscopes

Vibrating ring gyroscopes have a symmetrical structure and offer many advantages over other gyroscope designs. They have high accuracy, high resolution, better thermal stability, better matching of operating frequencies, low zero output ratio, and increased sensitivity [40]. The basic design of a MEMS vibrating ring gyroscope is shown in Figure 1.11. It consists of an outer ring with eight springs supported by a circular anchor placed in the middle.

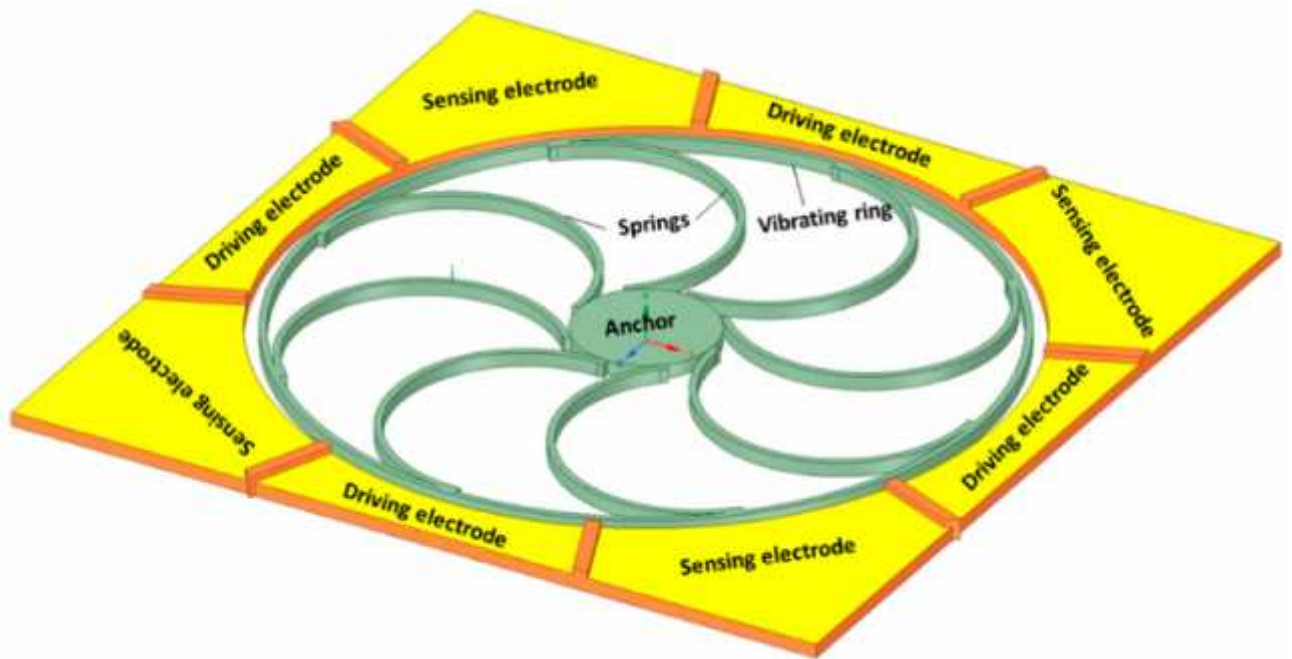


Figure 1.11 - Schematic representation of the basic design of a vibrating ring gyroscope.

The principle of operation of a vibrating ring gyroscope is illustrated in Figure 1.12. The vibration structure of the gyroscope is surrounded by eight driving and sensing electrodes. The driving electrodes provide continuous oscillations in the direction of the driving axis. The movement of the ring is clearly visible in the direction of travel. However, there is no movement along the sensing electrodes. When the gyroscope is subjected to an external rotation, the elliptical shape of the oscillation mode is now transferred to the sensing electrodes. When the rotation is applied to the device, the primary vibration induces a secondary vibration in the reading direction due to the generated Coriolis force. The sensing electrodes sense the change in displacement.

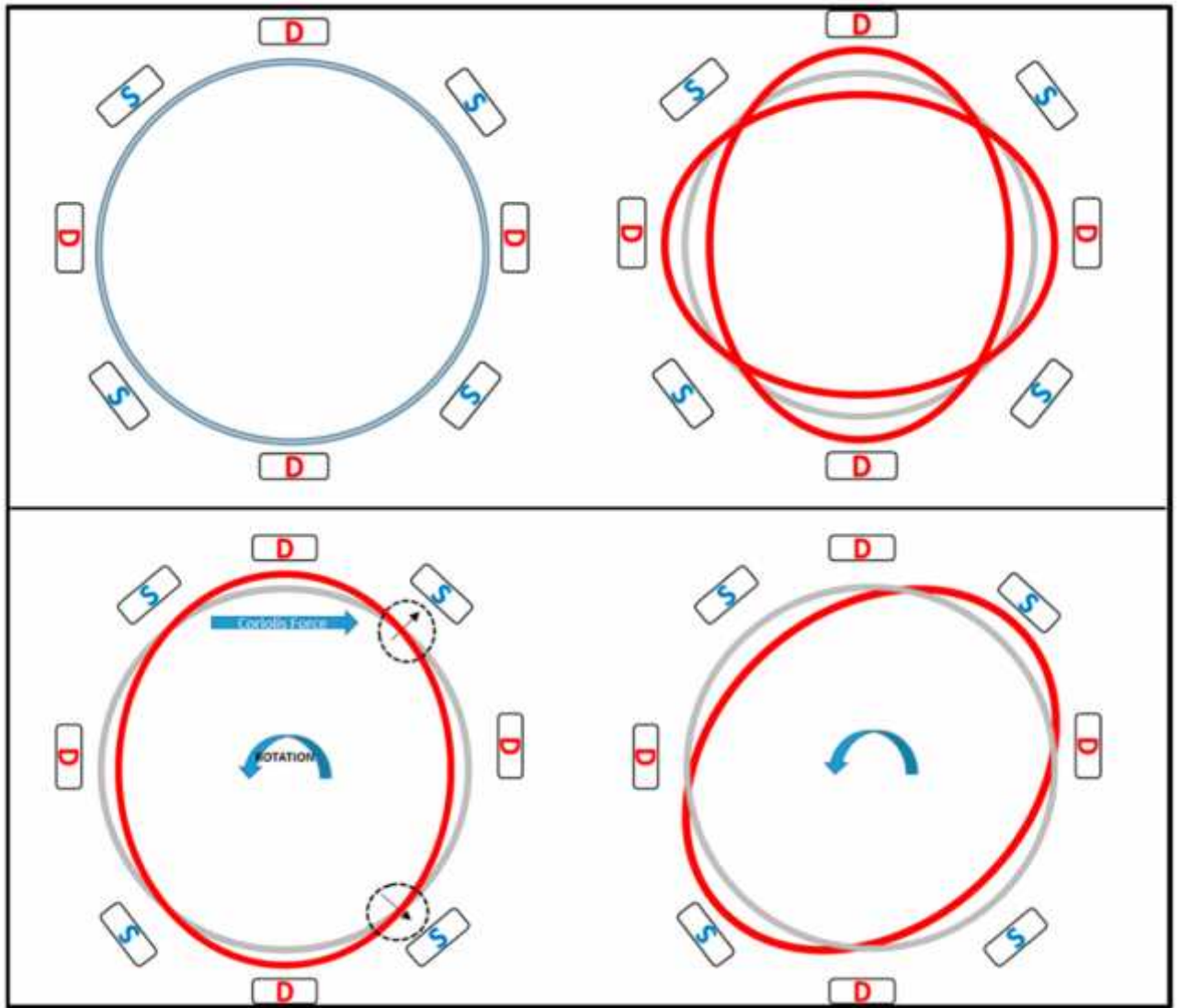


Figure 1.12 - Schematic demonstration of the operation of a vibrating ring gyroscope.

The General Motors Corporation invented the vibrating ring gyroscope [41]. The ring structure was considered as a vibrating element with high quality radial vibrations. The ring structure was designed to be electrically conductive. Several electrodes were placed around the ring structure for the driving and sensing mechanism, as shown in the schematic in Figure 1.13. The ring structure was supported by a centrally placed support pillar, and the ring structure was driven by electrostatic driving electrodes. As the structure rotated, the energy of the first vibrating mode caused it to move in a 45-degree direction from its position, and the

sensing electrodes, which were placed at a 45-degree angle with the driving electrodes, sensed this capacitive motion of the vibrating ring.

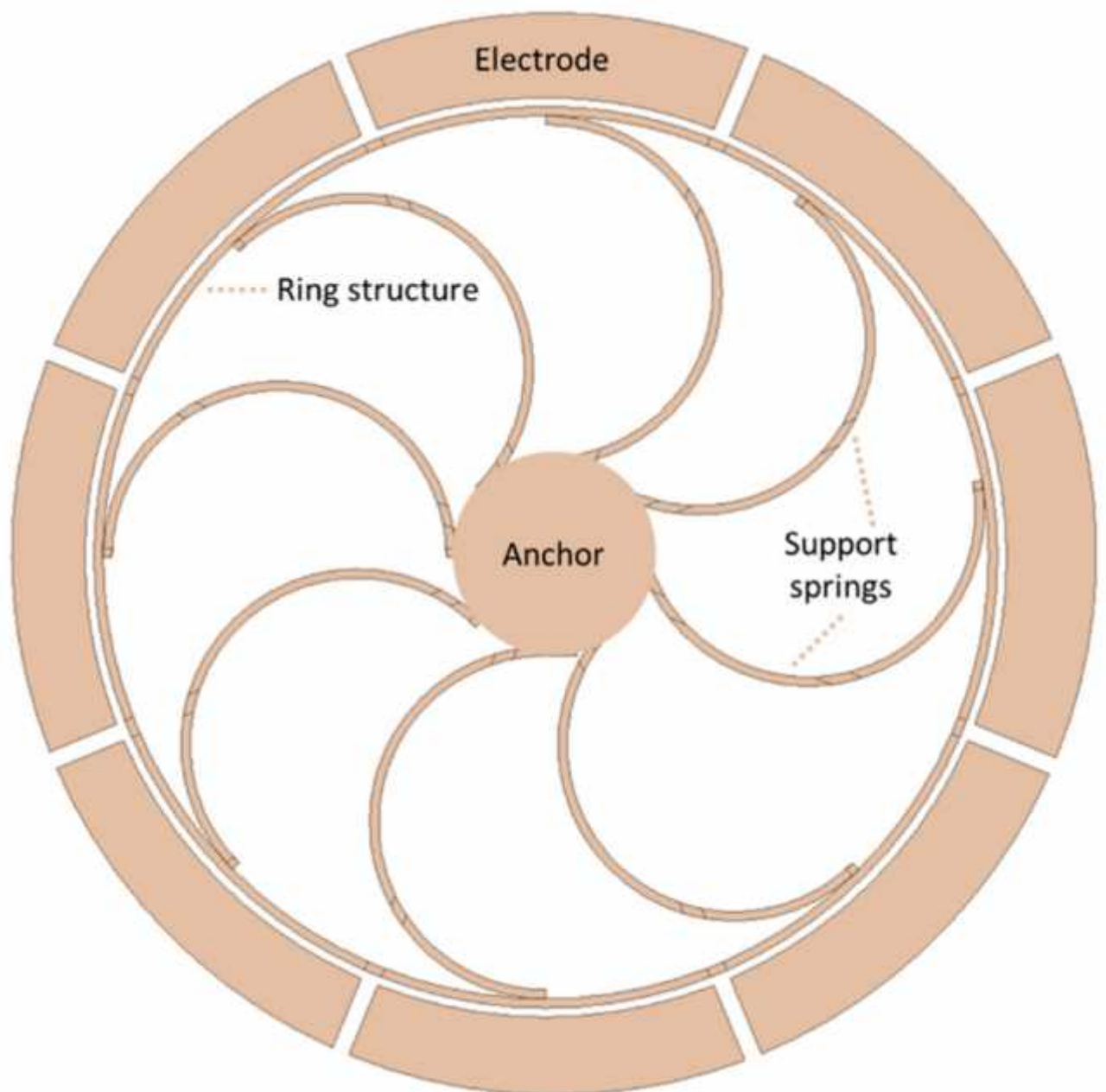


Figure 1.13 - Schematic view of a novel vibrating ring gyroscope developed by General Motors.

In 1998, a research team at the University of Michigan reported the first development of a micromachined polysilicon vibrating ring gyroscope [42]. The ring structure was 30 to 40 microns thick, and the gap between the ring and the electrode

was 0.9 microns. Due to the symmetrical design, the control and sensing frequencies were almost identical, resulting in high sensitivity. The same researchers [43] presented an in-depth study of vibrating ring gyroscopes for scale limiting and combined micromanufacturing technologies such as bulk and surface micromachining. The structural layer of the vibrating ring gyroscope with a thickness of 30 μm was fabricated using polysilicon trench filling microfabrication technology with a gap between the ring and the electrode of 0.9 μm . The ARW was fixed at 0.05 deg/ h, and the overall sensitivity and performance level increased significantly. Achieving the high performance of the vibrating ring gyroscope was due to many reasons, including the choice of polysilicon substrate, smaller ring-to-electrode gap, quality factors, and dry-etch manufacturing technology.

The same research group [44] presented a polysilicon vibrating ring gyroscope with a high aspect ratio, manufactured using dry release microfabrication technology. The height of the structure of the vibrating ring gyroscope was 80 μm . The advantage of the dry release technology was the use of a single wafer and the formation of electrically insulated electrodes of the same height as the ring structure. The sensitivity of the vibrating ring gyroscope was measured as 200 $\mu\text{V}/\text{deg}/\text{s}$ in a dynamic range of ± 250 deg/s under low vacuum conditions. The Q-factor was recorded as 1200 and the motion amplitude was measured at 0.15 μm with a parasitic capacitance of 2 pF at the sensing node.

A high-performance vibrating ring gyroscope was fabricated using the (111) orientation of a single crystal silicon wafer. The vibrating ring structure of single crystal silicon was deposited on a glass substrate with a high aspect ratio [45]. The ring radius was 1.35 mm, and the thickness of the structural layer was 150 μm . The DRIE process made it possible to obtain a 480 μm thick silicon wafer (111) and etch it. The electrode ring and structure were etched down to 150 microns. Next, the wafer was etched on the back side to release the structural layer using reactive ion etching. The tested gyroscope achieved a Q factor of 12,000, and the nonlinearity was measured at 0.02%, with a higher sensitivity of 132 mv/deg/s with high resolution. A

new vibrating ring gyroscope with S-shaped support springs was presented by Kou et al. [46]. The ring structure was supported by eight S-shaped symmetrical support springs with a centrally mounted support on a circular pillar, as shown in Figure 1.14. The ring structure was driven electrostatically by the drive electrodes, and the rotational motion was sensed by the sensing electrodes. The entire gyroscopic structure was fabricated using a high aspect ratio microfabrication process. To evaluate the overall gyroscopic performance of the gyroscope, tests were conducted at atmospheric pressure. The operating resonant frequencies were measured at 9.844 kHz for motion and 9.865 kHz for sensing. The Q-factor was 186 and 163 for driving and sensing, respectively. The zero-displacement instability was recorded at 0.017 deg/s, and the ARW was 0.14 deg/ h.

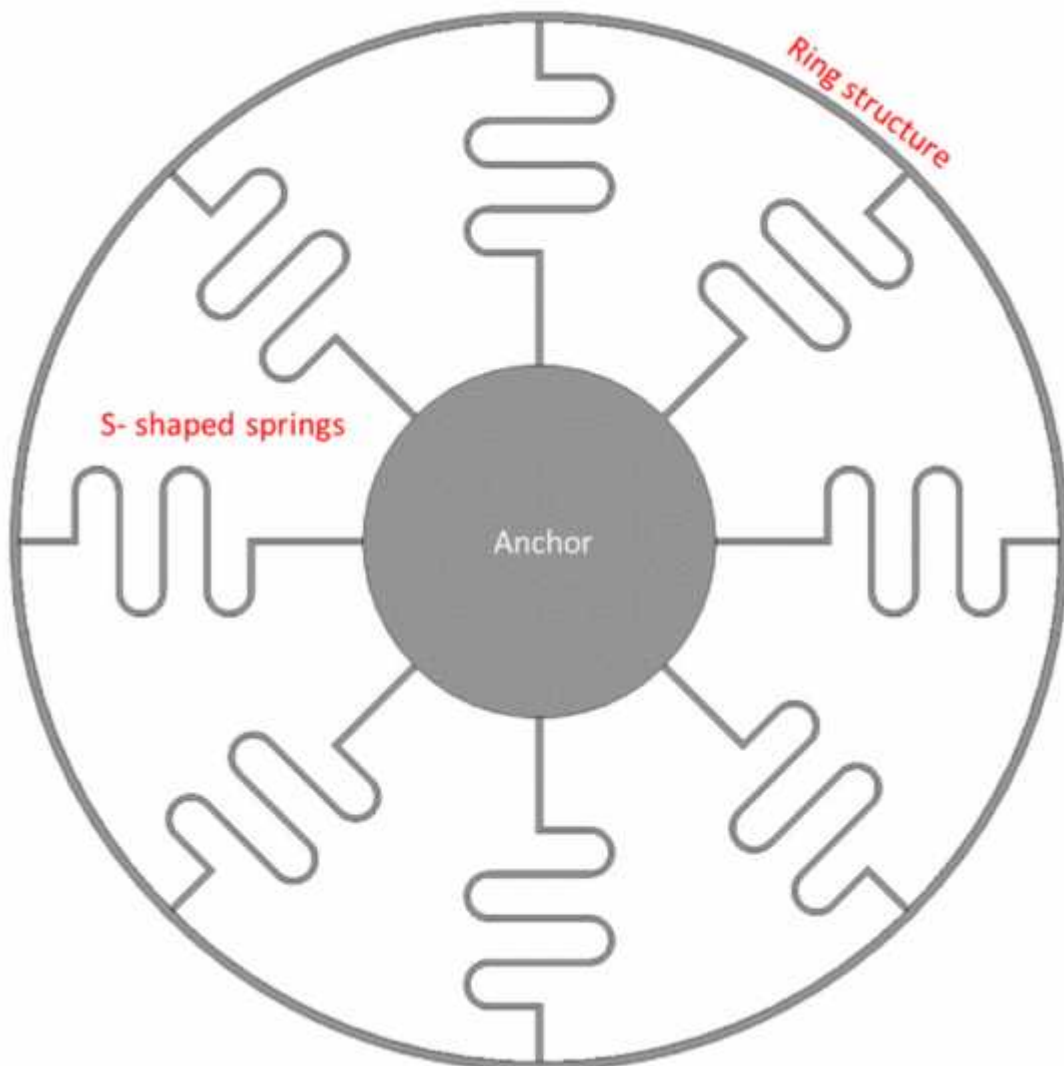


Figure 1.14 - Schematic view of eight S-shaped support springs in a vibrating ring gyroscope

Kou et al. built on their work and further investigated the solid-state vibrating ring gyroscope to increase the level of sensitivity [47]. The solid-wave gyroscope has many advantages, such as high reliability, wide dynamic range, and higher mechanical sensitivity. An exhaustive finite element analysis was performed to design the gyroscope and model the resonant frequency and sensitivity analysis. The relationship between the design parameters and the numerical sensitivity model was carefully analyzed. The calculated resonance frequency was fixed at 6.04 kHz, and the mechanical sensitivity was measured at $0.0036 \mu\text{m}/\text{deg/s}$.

Syed et al. [48] presented a case study of the migration of a MEMS vibrating ring gyroscope design from a multi-step complex fabrication process to a simple, cost-effective process. Two different approaches to the design of the MEMS vibrating ring gyroscope were considered. In the first design, the multi-vibration ring structure had C-shaped support springs connected to each other and was also supported by an internal anchor. However, in the second design, the multi-vibration rings with C-shaped support springs were connected and supported by an external anchor. In the first design, there were certain production constraints to fill the entire area, so the area was filled with more pillars. The second design provided better results for gyroscopic operation. The second design provided better sensitivity, a simple microfabrication process, ideal wine glass vibration modes, and high impact resistance.

A double U-beam ring vibration gyroscope was created by Cao et al. [49]. The design of the device was developed using a mathematical model and finite element modeling. The gyroscope structure consists of a circular ring connected to eight double U-shaped support springs connected to a centrally placed anchor. Twenty-four electrodes were placed around the ring structure to vibrate the ring using driving

electrodes and to measure changes in capacitance due to changes in displacement using sensing electrodes. A schematic diagram of a double U-beam vibrating ring gyroscope is shown in Figure 1.15. The microfabrication was done with silicon on glass technology with deep reactive-ion etching. The designed, simulated resonant frequencies for driving and sensing were 9.609 kHz and 9.615 kHz, respectively. The gyroscope was tested for actual performance; the tested resonant frequencies for control and sensing were 9.124 kHz and 9.146 kHz, respectively, which were lower than the calculated frequencies. The bias instability was measured at 8.86 deg/hr and the ARW at 0.78 deg/ h.

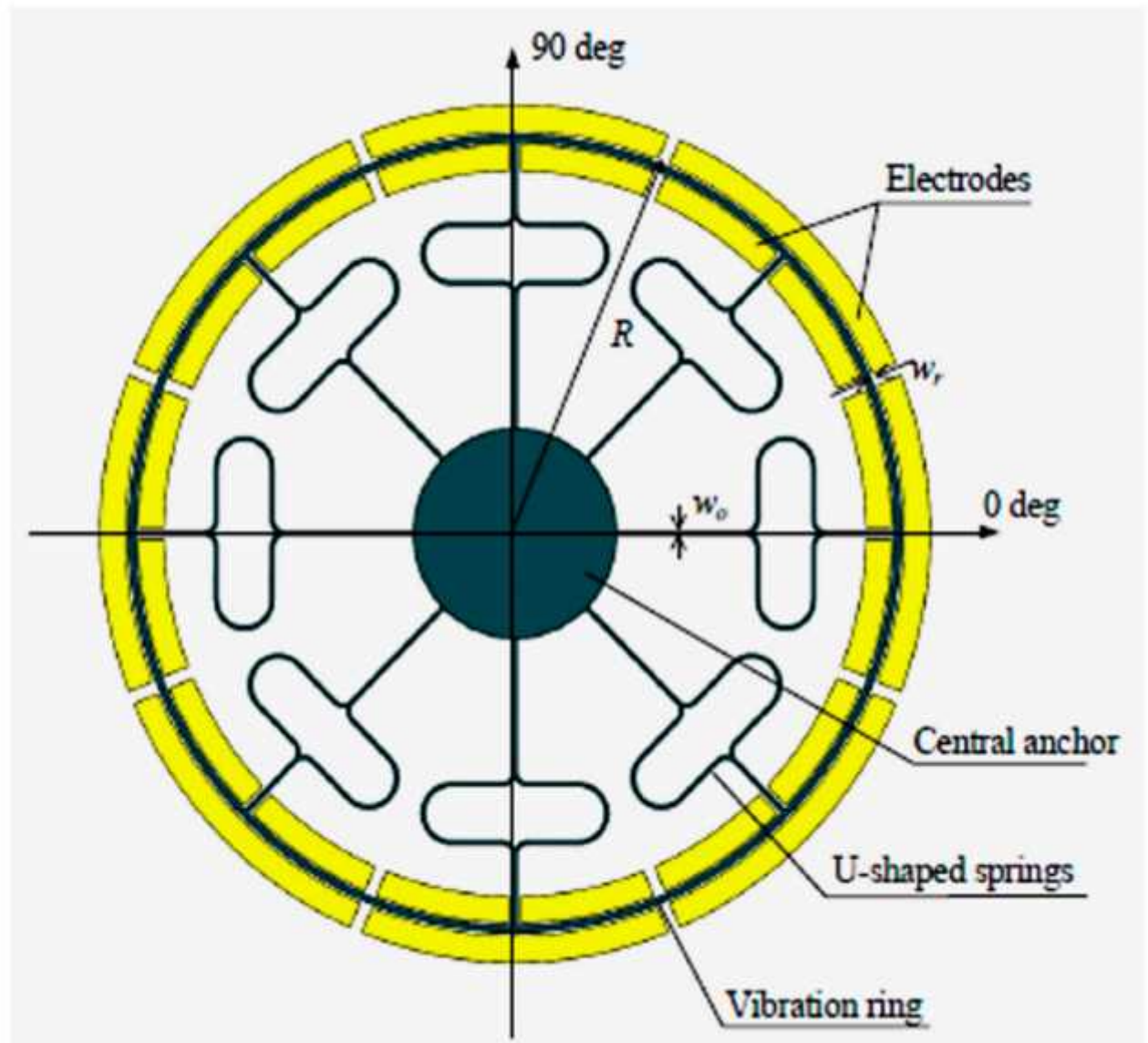


Figure 1.15 - Schematic view of MEMS double U-beam vibrating ring gyroscope [56].

A new design of a multi-ring vibration gyroscope was created in [50]. The design had two sets of ring structures: inner and outer rings. Multiple rings increased sensitivity. The ring structure with C-shaped support springs was connected to an external fixed anchor. The proposed design of the multi-ring vibration gyroscope is shown in Figure 1.16. The modeled resonant frequency was 40.40 kHz. However, when the device was characterized, the measured resonant frequency was 36.67 kHz. The difference between the calculated and tested resonance values was less than 4.0 kHz. The reason for the discrepancy was due to microfabrication errors, such as critical dimensional losses and sidewall angle.

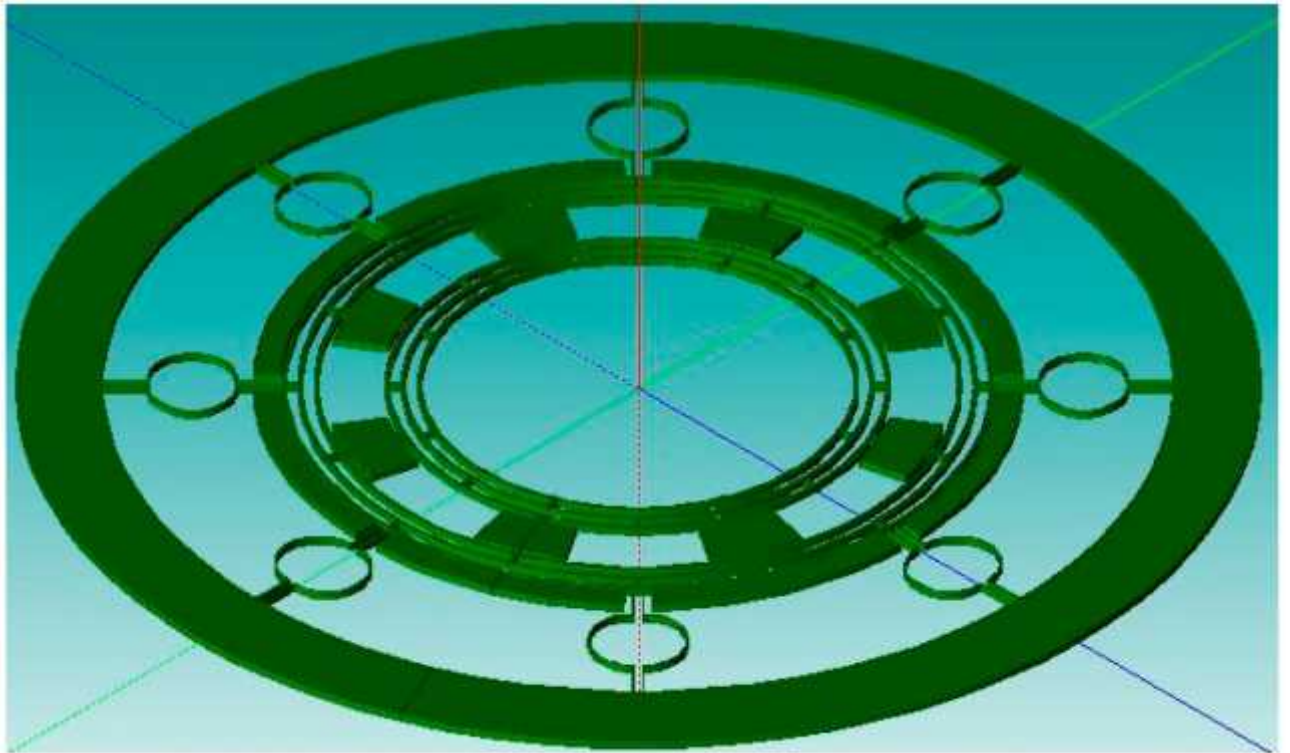


Figure 1.16 - Design of a multi-ring vibrating gyroscope [57].

Liang et al. [51] developed a gyroscope with a MEMS vibrating ring that was attached to a piezoelectric film. The piezoelectric film covered the circumference of the vibrating ring to adjust the gyroscope's stiffness. The proposed piezoelectric film increases sensitivity by controlling forced oscillations and parametric resonance. The increase in bias voltage and piezoelectric voltage can increase the amplitude response of the gyroscope. Because of the forced oscillations, the amplitude response of the sensing is more significant because of the forced oscillation rate. When the oscillation rate decreases, other parameters are affected. The best way to maximize sensitivity is to design the gyroscope oscillation rate close to the optimal values. The same research group [52] further studied the nonlinearity behavior of a vibrating ring gyroscope. The results were obtained by using a nonlinear model to identify couplings with geometric and structural coupling. It was found that the cubic stiffness nonlinearity has a significant impact on the coupling between the control and sensing modes.

1.4.4 Multi-Axis Gyroscopes

A new two-dimensional micromechanical gyroscope was developed by Fujita et al. [53]. The new design, shown in Figure 17, included four cantilever plates that were placed over a glass substrate with four fixed electrodes. When a rotation was applied to the micro gyroscope, the motion was caused by the Coriolis force and detected capacitively as the displacement between the cantilever and the fixed electrodes changed. They suggested that the control and sensing frequencies should be matched to improve the overall sensitivity of the gyroscope. The sensitivity recorded for this two-dimensional gyroscope was 0.1 mV/deg/s.

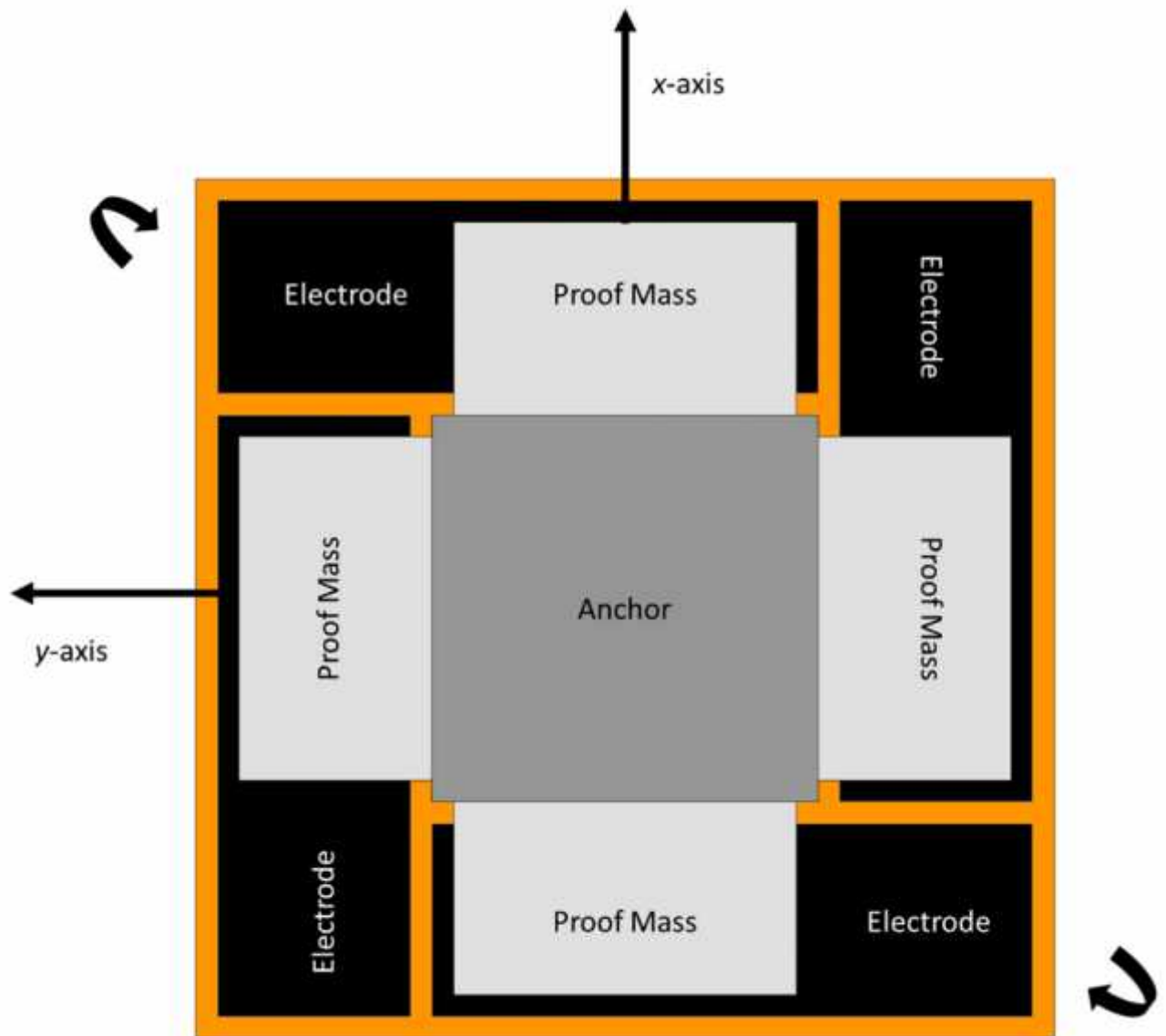


Figure 1 - Schematic diagram of novel two-dimensional micromachined gyroscope developed by Fujita et al.

In 1997, a biaxial micromechanical velocity gyroscope was presented at the IEEE Transducers 97 conference [54]. The gyroscope had a polysilicon disk with a thickness of $2\ \mu\text{m}$ and a diameter of $0.3\ \text{mm}$, placed at a height of $1.6\ \mu\text{m}$ above the substrate. The disk structure was supported by four beams that were connected to four anchors to support the disk structure. The beams were designed to provide torsional suspension. The device operated in angular resonance around the z-axis, and rotation around the x-axis caused a Coriolis reaction on the y-axis. Due to the symmetrical structure of the gyroscope, any rotation in the y-axis caused a Coriolis

reaction in the x-axis. This change was sensed capacitively by sensitive electrodes placed under the disk structure. A schematic representation is shown in Figure 1.18. The AWR was significantly higher due to the mismatch of the resonant and tuning frequencies, and the ARW decreased to 2 deg/ h from 10 deg/ h, but with high sensitivity along the transverse axis.

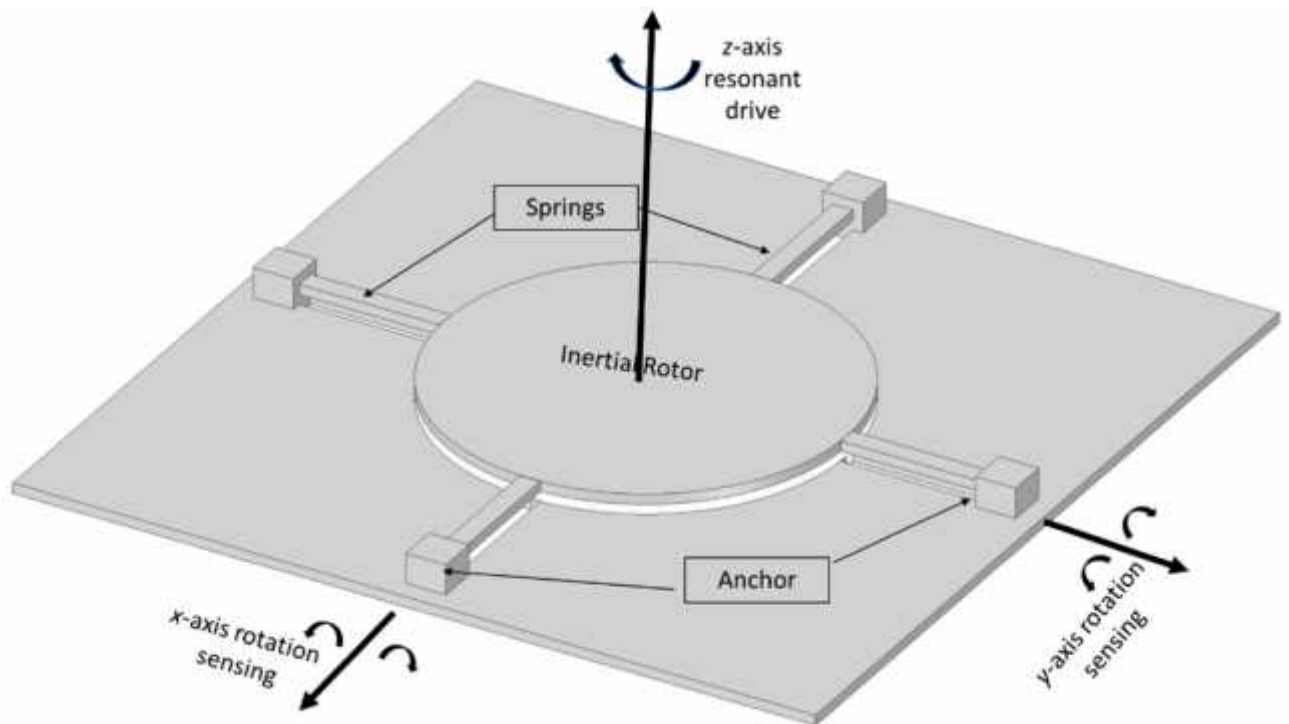


Figure 1.18 - Schematic diagram of a dual-axis micromachined vibrating gyroscope.

NASA's Jet Propulsion Laboratory presented its work on the manufacture, design, and packaging of a microgyroscope for space applications [55]. The microgyroscope had a 7 Hz separation frequency between control and sensing modes, a scale factor of 24 mV/deg/s, a displacement stability of 70 deg/h, and a ARW of 6.3 deg/ h. The entire system consisted of a micro gyroscope, a preamplifier, a power converter, and a summing circuit.

In 1998, Kang et al. presented a tunable micro-machine-controlled gyroscope [56]. The device had a polysilicon structure, two suspended microplates

electrostatically vibrated in a comb-like structure in an antisymmetric direction, and two electrodes were placed under the plate structure. When an external rotation was applied to the device, a Coriolis acceleration developed, which caused the plates to move in the opposite direction or away from the lower electrodes. This change in capacitance was perceived by the lower electrodes.

A research team from the University of California has developed a four-mass gyroscope with integrated MEMS rate. The proposed quad-mass gyroscope design offers a dynamically balanced and highly symmetrical structure. This vacuum-sealed, four-mass gyroscope achieved a high-quality factor of over one million in the motion and sensing directions. The gyro operated at a resonant frequency of 2 kHz. The gyroscope operated with mode-matching and showed a linear response in the range of ± 450 deg/s and a bandwidth of 100 Hz [57,58]. Zotov et al. presented the first mechanical frequency-modulated angular velocity gyroscope. The presented gyroscope is based on a four-mass gyroscope with a symmetrical structure along the X-Y axes. The high range angular velocity sensor was digitally tested using a two-phase closed loop. The device maintained a quality factor of more than one million in the direction of motion and sensing in the temperature range from -40 °C to 100 °C [59].

Senkal et al. [22] described a two-mass full-angle MEMS gyroscope based on the concept of Foucault's double pendulum. A schematic representation of this gyroscope is shown in Figure 1.19. The gyroscope has a symmetrical design along the X-Y axes. The dual-axis gyroscope operated at a frequency of 2.7 kHz with a quality factor of more than 100 k in both the motion and sensing modes. Minotti et al. [60] developed a three-axis frequency-modulated MEMS gyroscope. The yaw and pitch rates were demonstrated by coupling to two MEMS structures that were fabricated using a 24 μm thick structural layer deposition process. The devices showed a stable high scale factor.

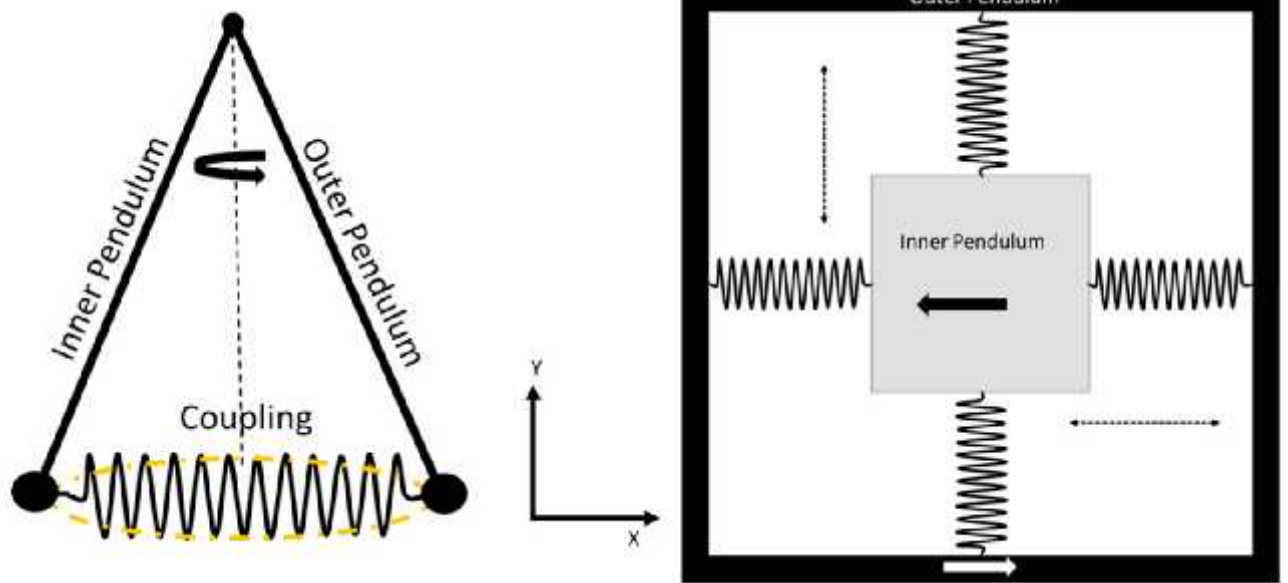


Figure 1.19 - Schematic diagram of dual Foucault pendulum gyroscope. Two Foucault pendulums vibrate in antiphase motion

Table 1 in the Appendix shows the chronology of the most common MEMS vibration gyroscopes and their development over the years. The Charles Stark Draper Laboratory initially began research on developing a vibration structure for the gyroscope. Later, many other institutions introduced different designs that provided better overall gyroscopic performance.

SECTION 2. THE RATE-INTEGRATING MEMS VIBRATORY GYROSCOPES

2.1 Principle of operation of the rate-integrating MEMS vibratory gyroscopes

Coriolis Vibrating Gyroscopes (CVGs) are divided into two classes, depending on the nature of the two modes of vibration. In the first class, the modes are different. An example of this class are beam and tuning fork gyroscopes, in which the controlled mode is the normal oscillation of the tuning fork - the primary mode, while the secondary or readout mode is the torsional oscillation of the tuning fork about its axis of symmetry. The primary and secondary modes of the beam and tuning fork resonators are shown in Fig. 2.1.

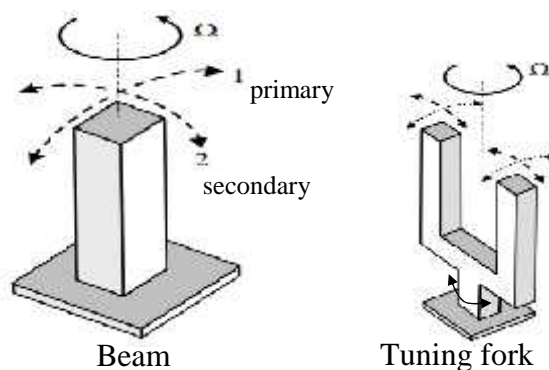


Fig. 2.1. CVG resonators of the first class

In the second class, the two modes are identical, being two orthogonal modes (modes of the same natural frequency) of an axisymmetric elastic body. Examples are the vibrating cylinder, hemispherical shell, and ring, as depicted in fig. 2.2, and in fact, any axisymmetric shell obtained as a body of rotation.

| | | | | | | | |
|-----------------------|------------------------|--|--|---|----------------|--------------|--------------|
| <i>ACS Department</i> | | | | <i>Name</i> | | | |
| <i>Performed.</i> | <i>D. Starozhytnyk</i> | | | <i>The Rate-Integrating MEMS Vibratory Gyroscopes</i> | <i>N..</i> | <i>Page.</i> | <i>Pages</i> |
| <i>Supervisor</i> | <i>V. Chikovani</i> | | | | | 42 | 9 |
| <i>Consultant</i> | <i>V. Chikovani</i> | | | | 402 151 | | |
| <i>S. controller.</i> | <i>V. Chikovani</i> | | | | | | |
| <i>Dep. head</i> | <i>Yu. Melnyk</i> | | | | | | |

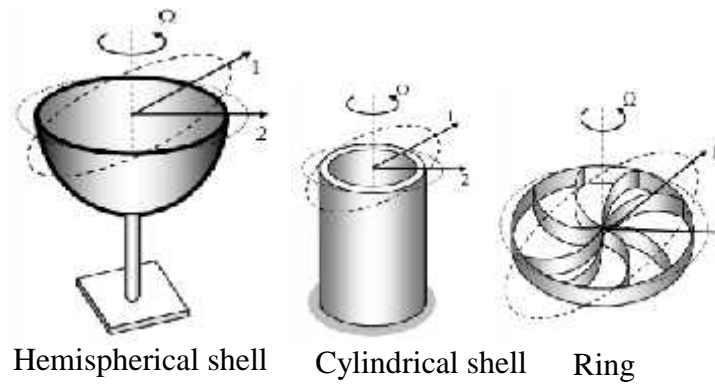


Fig. 2.2. CVG resonators of the second class

The operation principle of a Coriolis vibratory gyroscope is based on the sensitivity of elastic resonant structures to the inertial rotation.

One of the most important parameters of resonators is its quality factor (Q-factor), which, in the main, depends on the properties of the material from which the resonator is manufactured and on a degree of an asymmetry of its shape. Q-factor is determined as follows:

$$Q = \omega_r \tau / 2 = \pi f_r \tau, \quad (2.1)$$

where ω_r and f_r are circular and cyclic resonant frequency of a resonator, τ is a time constant, i.e. time of free oscillations amplitude damping e times, where $e = 2.718$.

There are two known modes of CVG operation: the first one is a force-rebalance mode, where Coriolis force arising due to rotation is compensated for by the negative feedback control loop, holding the vibratory standing wave in a fixed position close to an excitation electrode, and hence, it rotates together with a gyro. In this case, the signal that compensates for the Coriolis force is proportional to the angle rate. It is the so-called rate mode of CVG operation. This mode of operation has been described in many works, for example [61–64].

The second mode is a rate-integrating one (or whole angle mode), where Coriolis force is not compensated for. The quadrature signal is only compensated for to reduce measurement errors. In this mode of operation, Coriolis force causes rotation of the vibratory standing wave relative to the gyro and an angle of its rotation is proportional to an angle of a gyro rotation relative to the inertial space. The coefficient of proportionality between the angle of a gyro rotation relative to the inertial space and the angle of the standing wave rotation relative to a gyro is called the Bryan coefficient or angular gain coefficient. This mode of operation has also been described in many works, for example [61, 62, 65, 66]. The first and second modes of operation have been combined in dual-mode CVG [67].

Relatively recent investigations [68–70] conducted in Ukraine have led to the development of a third, differential, mode of CVG operation, which complements the first two modes. The differential mode of operation is realized by holding the standing wave between the electrodes using two drive signals applied along two axes, located at the angle of 45° to each other. In this case, two measuring channels X and Y are formed, each of which provides a signal proportional to an angular rate with opposite signs $+\Omega$ and $-\Omega$. The differential mode of operation has additional capabilities to compensate for the effects of both internal and external destabilizing factors when measuring angular rate [71, 72].

2.2 Rate Mode Principle of Operation

In a vibrating beam gyroscope, which consists of one end fastened beam made of any elastic material (see fig. 2.1), the drive (primary) mode is a flexural vibration that can be induced by any actuator (piezoelectric, electrostatic, or electromagnetic). A secondary mode vibration (sense-mode), normal to the drive mode vibration, is induced in the beam due to the Coriolis force arising in the presence of the rotation about the longitudinal axis of the beam, shown in fig. 2.1. The secondary vibration can be sensed by a sensor, which can also be piezoelectric, electrostatic,

electromagnetic, or optical. Coriolis force vector F_c induced by rotation is determined as the following vector product:

$$\mathbf{F}_c = 2m[\mathbf{h} \times \mathbf{V}], \quad (2.2)$$

where m is an effective vibrating mass, \mathbf{h} is a rotation angle rate vector, and \mathbf{V} is a linear velocity vector of mass points during vibration.

A length (a value) $|\mathbf{F}_c|$ of the vector \mathbf{F}_c is determined to be:

$$|\mathbf{F}_c| = 2m|\mathbf{h}||\mathbf{V}|\sin(\angle(\mathbf{h} \mathbf{V})), \quad (2.3)$$

where $|\mathbf{h}|$ is a length of a rotation angle rate vector, $|\mathbf{V}|$ is a length of a linear velocity vector, $\angle(\mathbf{h} \mathbf{V})$ is an angle between \mathbf{h} and \mathbf{V} vectors.

In the particular case of the vibrating beam, the angle between these two vectors is equal to 90° , hence $\sin(\angle(\mathbf{h} \mathbf{V})) = 1$. The direction of a vector \mathbf{F}_c is determined as perpendicular to the direction of a vector \mathbf{h} and of a vector \mathbf{V} . It means that Coriolis force induces vibration in the direction of secondary vibration, as depicted in fig. 2.1, i.e. perpendicular to the drive (primary) vibration.

Let a beam is driving at the beam's resonant frequency ω_r with an amplitude A along the X direction, then elementary mass point trajectory in the X direction is:

$$x(t) = A \cos(\omega_r t). \quad (2.4)$$

Linear velocity during vibration is:

$$V(t) = \dot{x}(t) = A\omega_r \sin(\omega_r t). \quad (2.5)$$

For the Coriolis force that induces vibration in the perpendicular the X direction, the following expression can be obtained:

$$F_c = 2m \omega_r \Omega \cos(\omega_r t). \quad (2.6)$$

As can be seen from (2.6) the Coriolis force is an amplitude modulated signal, in which carrier frequency is a resonant frequency of the vibrating structure and its envelope is proportional to the angle rate measured. Coriolis force changes in phase

quadrature to the drive vibration phase. The coefficient of proportionality between the Coriolis force and the angle rate measured is called the rate CVG scale factor and it is equal to $SF=2mA\omega_r$. The bandwidth of a gyroscope is $1/\tau$, i.e. the more the Q-factor of the secondary mode of a vibrating structure, the less the bandwidth.

In the case of a tuning fork, two beams (tines) are vibrating out-of-phase to compensate for the moment acting on a stem. Under rotation along its axis of symmetry, there arise Coriolis forces which create a torsional moment M_c about a stem axis. This torsional moment is proportional to F_c and a distance L between the tines, increasing sensitivity to angle rate.

$$M_c = F_c L \quad (2.7)$$

For the second class CVGs, which resonators are bodies of rotation, effective vibrating mass in essence is a ring resonating on the second $n=2$ vibration mode, because zero and first modes are insensitive to the rotation.

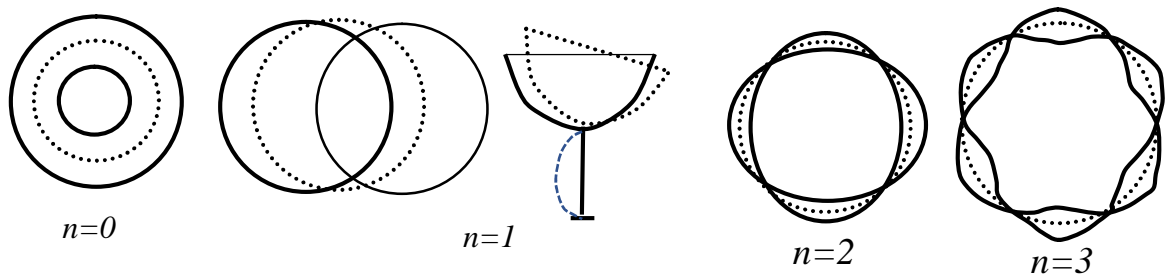


Fig. 2.3. Axisymmetric ring-like resonator's modes

The first three vibrating modes of an axisymmetric body of rotation are presented in fig. 2.3. The zero mode is a change in a ring diameter. The first mode is the vibration of the whole shell mounted on a stem. The second mode is a flexural vibration that is forming a standing wave with four nodes and four antinodes located through the angle 45^0 along a circumferential coordinate. The third mode forms the standing wave with six nodes and six antinodes with the angle between them equal to 30^0 and so on. For the higher vibration modes $n=3, 4, \dots$ sensitivity to angle rate reduces. In most second class CVGs the second ($n=2$) vibration mode is used, as it has maximum sensitivity to angle rate.

Fig. 2.4 shows the standing wave on the second resonant mode of the ring-like resonator, which is characterized by four antinodes (maximum vibration amplitude)

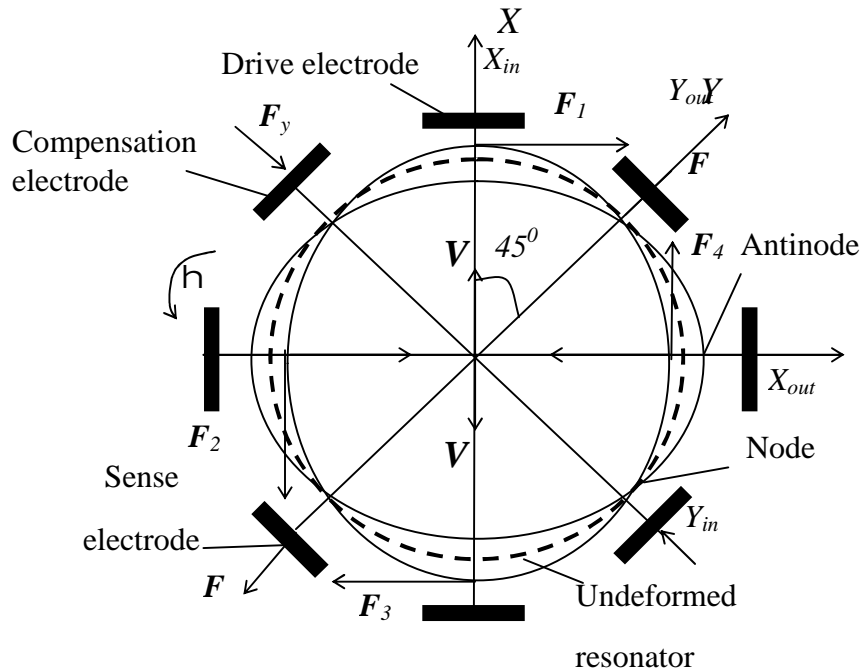


Fig. 2.4. A standing wave in a ring-like resonator and four nodes (minimum vibration amplitude) located under angles of 45° along circumferential coordinate.

Under resonator rotation with angle rate Ω , there arise Coriolis forces F_1 , F_2 , F_3 , F_4 (fig. 2.4), which generate a secondary (Coriolis) mode of vibration in the direction of the resultant force F_c . The resultant Coriolis force is proportional to angle rate, Ω . As can be seen from fig.2.4, the resultant Coriolis force is directed under the angle of 45° to the direction of drive vibration, hence it tries to excite vibration along the axis passing through the nodes. To increase the bandwidth, the node's vibration should be driven to null. For this aim node's vibration is measured and with the aid of a negative feedback control loop this vibration is damped by applying signal F_y equal by amplitude, but opposite by phase on the compensation electrode Y_{in} . The compensation signal F_y , which is measured, is proportional to Coriolis force and, hence, to angle rate Ω .

To minimize the resultant moment acting on a resonator from drive and compensation electrodes (X_{in} and Y_{in}) and increasing the measured signals from the

sense electrodes (X_{out} and Y_{out}) all diametrically opposite electrodes are short-circuited.

Due to compensation for the Coriolis force in a rate CVG, there is only one (primary) vibration mode in a resonator and a standing wave with its antinodes aligns along the two drive electrodes, having rotated together with the resonator with the same angle rate Ω . The elementary mass point trajectory for a rate CVG is an unmovable straight-line directed along a ring radius.

2.3 Rate-integrating mode principle of operation

Coriolis force caused by gyro rotation is not compensated for in the rate-integrating or whole angle mode of operation and as a consequence, this results in the superposition of the primary and secondary vibration modes and, as a result, in standing wave rotation, i.e. rotation of a set of its antinodes and nodes along the circumferential coordinate θ as a rigid body. This angle θ is proportional to the gyro rotation angle relative to the inertial space. The coefficient of proportionality between those two angles of rotation (of a standing wave and a gyro casing), which is called the rate-integrating CVG scale factor, is called the Brian coefficient [61] k or angle gain coefficient [73].

$$\theta(t) = -k \alpha(t); \alpha(t) = \int_0^t \Omega(\tau) d\tau, \quad (2.8)$$

where $\alpha(t)$ is a standing wave rotation angle relative to CVG casing, $\theta(t)$ is a CVG rotation angle relative to inertial space.

In absence of the gyro rotation resonator's elementary mass point motion trajectory, in the general case, is an ellipse shown in fig. 2.6. Ellipse parameters are designated as follows: a is a vibration amplitude, q is a quadrature amplitude caused

by the resonator's imperfection, ω_r is a resonant frequency, ϕ' is a vibration phase, θ is a standing wave orientation relative to the X-axis (drive electrode).

At a gyro rotation, the ellipse turns with the lag coefficient k . For cylinder resonator Brian coefficient k can be calculated using the expression [74]:

$$k = \frac{n}{n^2 + 1 + \frac{3}{n^2} \left(\frac{r}{h}\right)^2}, \quad (2.9)$$

where n is a mode number, r is a cylinder radius, and h is a cylinder height.

For example, for cylinder size: $r=13$ mm and $h=20$ mm, $k=0.38$, so, if CVG rotation angle relative to inertial space is 90° , then a standing wave rotation angle relative to CVG is $\theta = -0.38 \cdot 90^\circ = -34.2^\circ$. For the beam resonator shown in fig. 2.1, Brian coefficient for the first mode is $k=1$ [75]. This means that a standing wave is almost immovable relative to inertial space, hence, it can be a reference system inside a CVG for angle measurement relative to the inertial space.

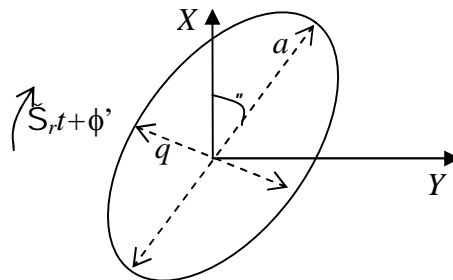


Fig. 2.5. Resonator's mass element motion trajectory in rate-integrating

The aim of a CVG control system in the rate-integrating mode of operation is to keep the standing wave parameters in process of operation at the following values [1]:

$$q=0, a = \text{const}, \phi'=0; \quad (2.10)$$

Parameter q is defined by difference in stiffness of the resonator that results in frequencies mismatch $\Delta\omega$. Besides, in order to obtain high accurate measurement of rotation angle, it needs to reduce Q-factor mismatch, ΔQ .

2.4 Two-dimensional pendulum model

To provide an adequate basis for the analysis of all CVG modes of operation, dynamic equations of oscillations should be generalized, including the components that determine the damping (Q-factor) and frequency (stiffness) mismatches and angular positions of their principal axes. Moreover, these equations should be convenient for engineering analysis and design of a control system for maintaining oscillations and measuring angle rate. Derivation of such generalized equations of the two-dimensional pendulum oscillations has been performed in [76] by D. Lynch for the mode $n = 2$. These equations, for the standing wave angle $\theta=0$, are written as follows:

$$\begin{aligned} \ddot{x} - k(2\Omega\dot{y} + \dot{\Omega}y) + \frac{2}{\tau}\dot{x} + \Delta\left(\frac{1}{\tau}\right)(\dot{x}\cos 2\theta_t + \dot{y}\sin 2\theta_t) \\ + (\omega^2 - k'\Omega^2)x - \omega_t(x\cos 2\theta_\omega + y\sin 2\theta_\omega) = f_x; \\ \ddot{y} + k(2\Omega\dot{x} + \dot{\Omega}x) + \frac{2}{\tau}\dot{y} - \Delta\left(\frac{1}{\tau}\right)(-\dot{x}\sin 2\theta_t + \dot{y}\cos 2\theta_t) + (\omega^2 - \\ k'\Omega^2)y + \omega_t(-x\sin 2\theta_\omega + y\cos 2\theta_\omega) = f_y; \end{aligned} \quad (2.11)$$

$$\omega^2 = \frac{\omega_1^2 + \omega_2^2}{2}; \quad \frac{1}{\tau} = \frac{1}{2}\left(\frac{1}{\tau_1} + \frac{1}{\tau_2}\right); \quad \omega\omega_\omega = \frac{\omega_1^2 - \omega_2^2}{2}; \quad \omega\left(\frac{1}{\tau}\right) = \frac{1}{\tau_1} - \frac{1}{\tau_2};$$

The parameters of equations (2.11) are shown in fig. 2.6, where the scheme of a two-dimensional pendulum is presented. The mass m in fig. 2.6 represents the elementary mass on the rim of the vibrating resonator; x and y are displacements along the X (primary) and the Y (secondary) resonator's axes; $\dot{\Omega}y$ and $\dot{\Omega}x$ are the angular acceleration; $k'\Omega^2$ is centripetal acceleration. There are also two axes with a

minimum ζ_1 and a maximum ζ_2 damping time of free oscillations, which is equivalent to the minimum Q_1 and maximum Q_2 quality factor of the resonator, since $Q = 1/2\zeta$. These equations take into account that a resonator has two axes with a maximum ζ_1 and a minimum ζ_2 resonant frequencies. Moreover, the axis of the minimum resonant frequency has an angle α with the X direction of the primary oscillations, and the axis of the minimum quality factor is the angle β with the direction of the primary oscillations, as shown in fig. 2.6. Forces f_x and f_y are a sum of control forces and forces arising due to the resonator's mass imbalance.

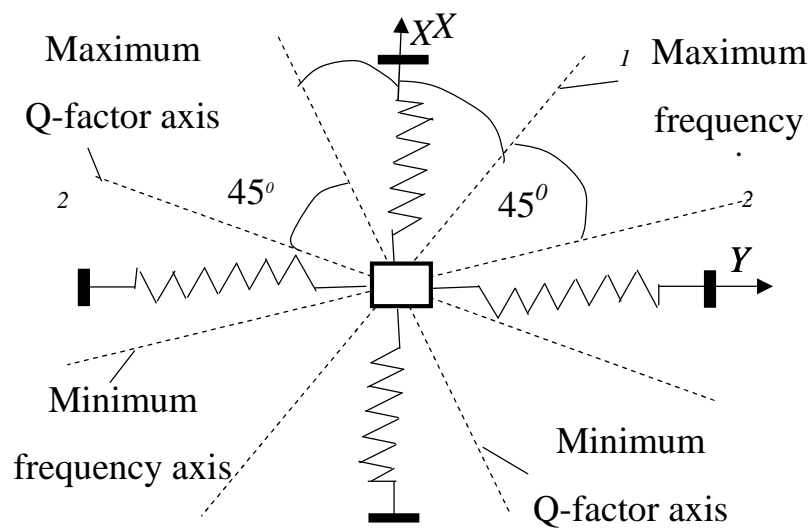


Fig. 2.6. Two-dimensional pendulum model

Equations (2.11) are normalized on the vibrating mass, so the right and left parts of the equations have the dimension of linear acceleration, and the forces in the right parts are specific ones (normalized by mass).

These equations, which describe the oscillations of the primary mode along the X -axis and the secondary mode along the Y -axis, are called equations in fast variables, as deviations from the equilibrium position of the resonator elementary mass at both X and Y coordinates occur with a sufficiently high frequency close to resonant one.

The terms due to the presence of the angular acceleration $\dot{\Omega}$ and centripetal acceleration Ω^2 are also presented in these equations, which will not be taken into account in future considerations due to their negligible values in comparison to other terms. Indeed, $\dot{\Omega}x$ is less than $\Omega\dot{x}$ as many times as the resonant frequency is greater than the maximum frequency of change of the measured angle rate, i.e. up to 100 times. The maximum value of Ω^2 in most applications is also less than $\Omega\dot{x}$ approximately 100 times.

Fig. 2.7 shows mass point trajectories when $q=0$ and $\Delta Q=0$, i.e., the resonator is ideal during standing wave rotation when measuring angle of rotation. This graph presents the resonator fast oscillations along a straight-line with the resonant frequency and, simultaneously, direction of the fast oscillations rotates with an angle rate proportional to the gyro rotation angle rate relative to the inertial space. Coefficient of proportionality is k and it is called the rate-integrating gyro scale factor.

Fig. 2.8 shows mass point trajectories when $q \neq 0$, but has a sufficiently small value equal to 0.1% of resonant frequency and $\Delta Q=0$. This graph presents an oscillation trajectory along an ellipse with quadrature component $q \neq 0$.

Fig. 2.9 shows mass point trajectories when $q=0$, and $\Delta Q \neq 0$, but has a sufficiently high value of about 50% of Q-factor.

Fig. 2.10 shows mass point trajectories when q has a large value, and $\Delta Q=0$, Fig. 2.11 shows mass point trajectories when $q \neq 0$, and $\Delta Q \neq 0$, but they have moderate values.



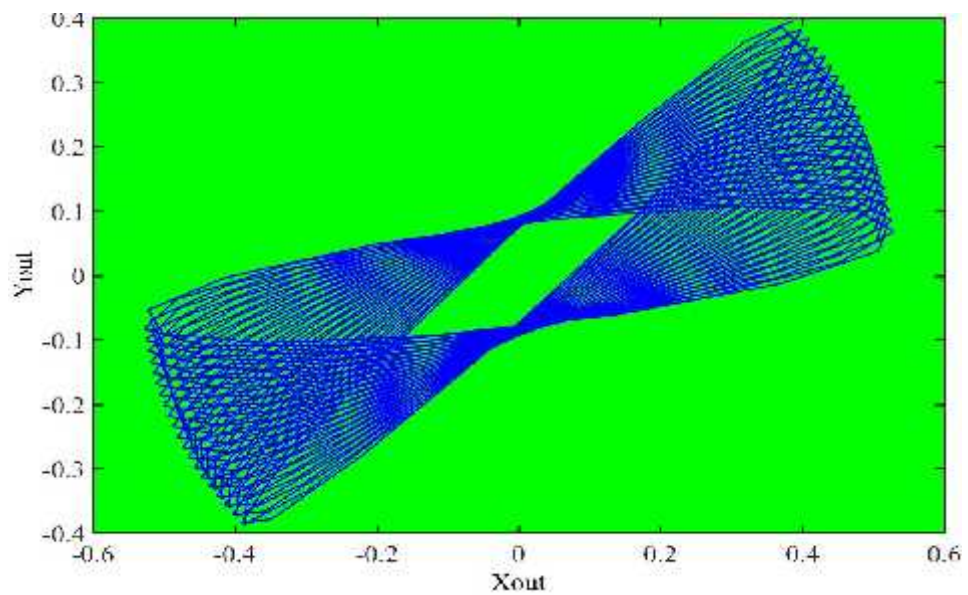
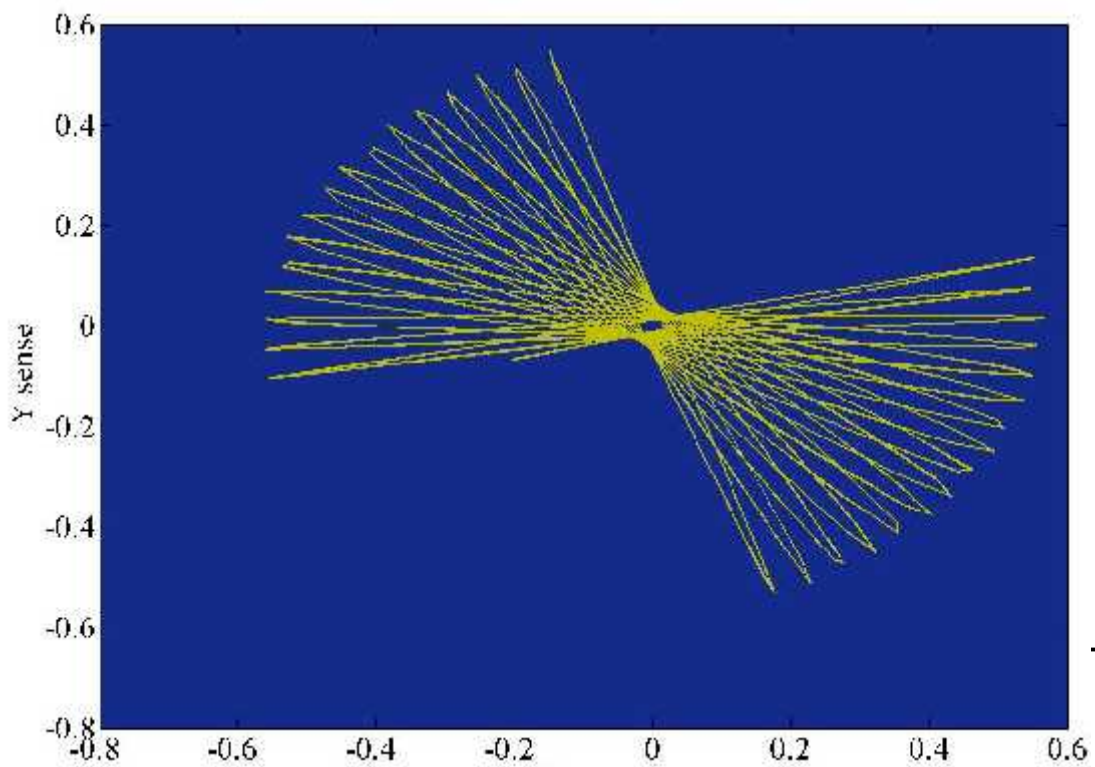


Fig. 2.8. Elementary mass point trajectory in a rate-integrating CVG with $q \approx 0$ and $\Delta Q \neq 0$, when $\Omega \neq 0$.



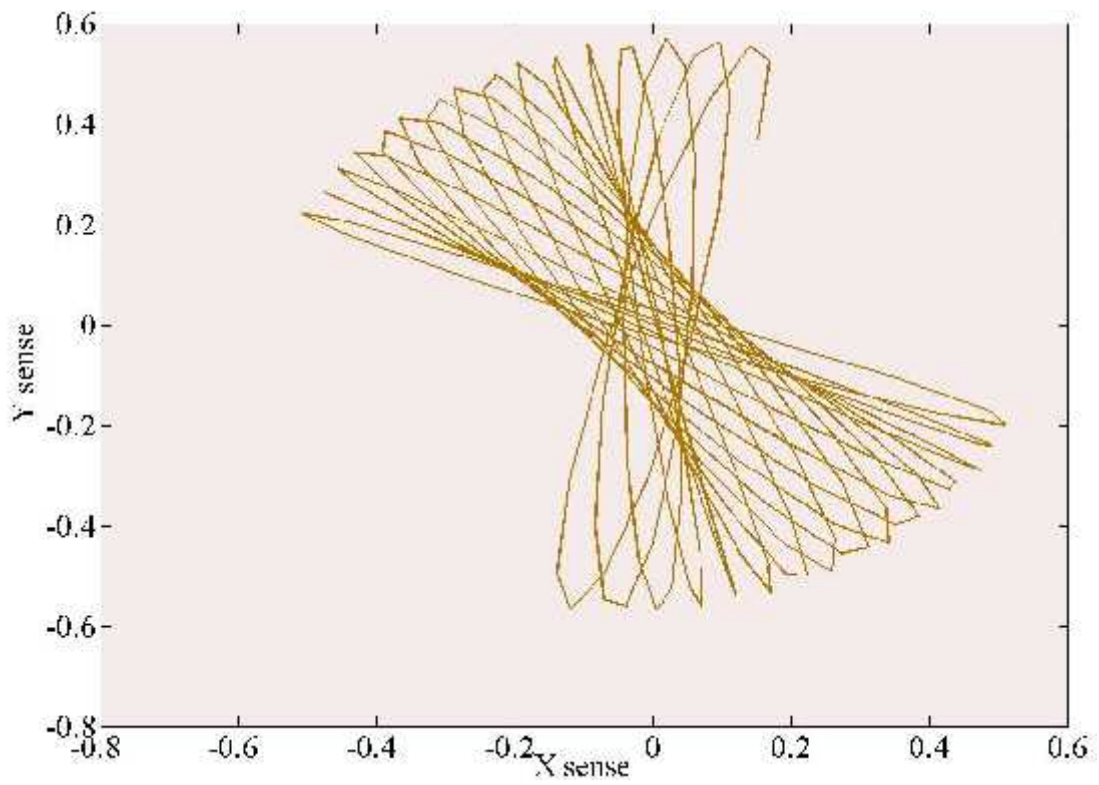
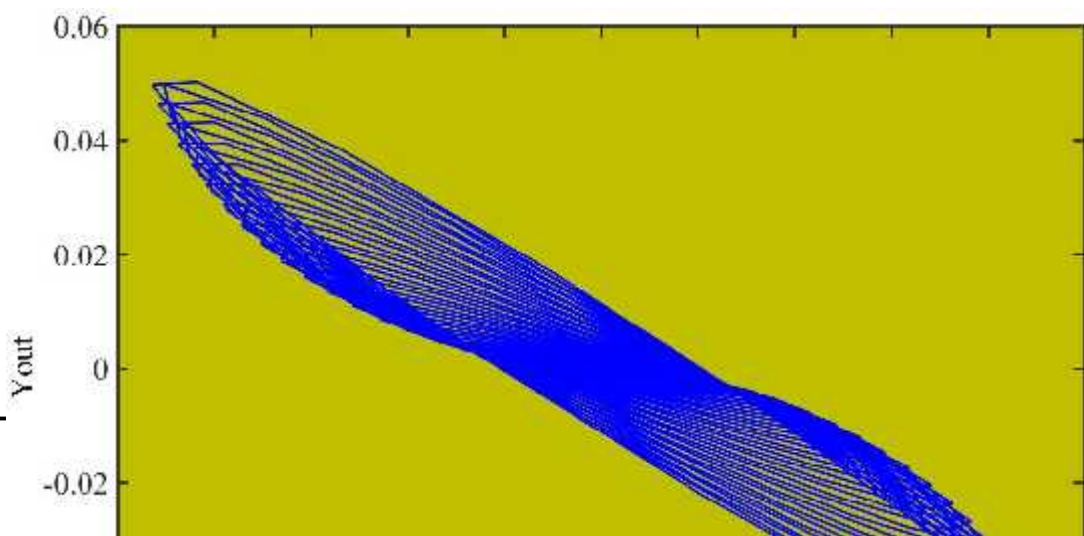


Fig. 2.10. Elementary mass point trajectory in a rate-integrating CVG with large q and $\Delta Q=0$, when $\Omega \neq 0$.



All these graphs have been obtained by simulation in Matlab.

SECTION 3. THE PERIODIC BIAS MODEL AND ITS CORRECTION

3.1. Dynamic equation of a resonator oscillation in slow variables

To represent the dynamics of oscillations in slow variables, the transformations of fast variables x, y into the four slow variables C_x, S_x, C_y, S_y are being introduced by the following relations:

$$\begin{aligned} x(t) &= S_x c_1 + C_x s_1 n \omega ; \\ y(t) &= S_y c_1 + C_y s_1 , \end{aligned} \quad (3.1)$$

Substituting (3.1) in (2.11 from the section 2)) and taking into account conditions for the existence of a standing wave in a resonator:

$$\begin{aligned} \dot{S}_x c_1 + \dot{C}_x s_1 &= 0; \\ \dot{S}_y c_1 + \dot{C}_y s_1 &= 0 , \end{aligned} \quad (3.2)$$

and after transformations and averaging over the period $T=2\pi/\omega$ of fast vibrations, taking into account the fact that during the period of fast vibrations the slow variables do not practically change, and the following relations are valid:

$$\begin{aligned} \frac{1}{T} \int_0^T s_1 dt &= 0; \quad \frac{1}{T} \int_0^T c_1 dt &= 0; \quad \frac{1}{T} \int_0^T s_1^2 dt &= \frac{1}{2}; \\ \frac{1}{T} \int_0^T c_1^2 dt &= \frac{1}{2}; \quad \frac{1}{T} \int_0^T s_1 c_1 dt &= 0, \end{aligned} \quad (3.3)$$

the four differential equations of the first order for slow variables can be obtained [76, 71]:

$$\begin{aligned} \dot{C}_x &\approx -\frac{d_x}{2} C_x + \frac{\omega_x^2 - \omega^2}{2\omega} S_x - \frac{d_x - 2k\Omega}{2} C_y + \frac{k_x}{2\omega} S_y - \frac{F_x}{2\omega}; \\ \dot{S}_x &\approx -\frac{\omega_x^2 - \omega^2}{2\omega} C_x - \frac{d_x}{2} S_x - \frac{k_x}{2\omega} C_y - \frac{d_x - 2k\Omega}{2} S_y + \frac{F_x}{2\omega}; \\ \dot{C}_y &\approx -\frac{d_y + 2k\Omega}{2} C_x + \frac{k_x}{2\omega} S_x - \frac{d_y}{2} C_y - \frac{\omega_y^2 - \omega^2}{2\omega} S_y - \frac{F_y}{2\omega}; \\ \dot{S}_y &\approx -\frac{k_x}{2\omega} C_x - \frac{d_x + 2k\Omega}{2} S_x - \frac{\omega_y^2 - \omega^2}{2\omega} C_y - \frac{d_y}{2} S_y + \frac{F_y}{2\omega}, \end{aligned} \quad (3.4)$$

| ACS Department | | | | Name | | | |
|----------------|-----------------|--|--|---|----------------|-------|-------|
| Performed. | D. Starozhytnyk | | | <i>The Periodic Bias Model And Its Correction</i> | N.. | Page. | Pages |
| Supervisor | V. Chikovani | | | | | 56 | 9 |
| Consultant | V. Chikovani | | | | 402 151 | | |
| S. controller. | V. Chikovani | | | | | | |
| Dep. head | Yu. Melnyk | | | | | | |

where

$$\begin{aligned} d_x &= \frac{2}{\tau} + h \cos 2(\theta - \theta_\tau); & d_y &= \frac{2}{\tau} - h \cos 2(\theta - \theta_\tau); \\ d_x &= h \sin 2(\theta - \theta_\tau); & h &= \frac{1}{\tau_1} - \frac{1}{\tau_2}; & k_x &= \omega_1^2 - \omega \Delta \omega \cos 2(\theta - \theta_\omega); \\ k_y &= \omega_1^2 + \omega \Delta \omega \cos 2(\theta - \theta_\omega); & k_x &= -\omega \Delta \omega \sin 2(\theta - \theta_\omega); \end{aligned} \quad (3.5)$$

Based on these designations, which have been written down for any arbitrary standing wave angle θ , the equations (2.11) in fast variable can be rewritten in a more compact form:

$$\begin{aligned} \ddot{x} - 2k\Omega \dot{y} + d_x \dot{x} + d_x \dot{y} + k_x x + k_y y &= f_x; \\ \ddot{y} + 2k\Omega \dot{x} + d_y \dot{y} + d_x \dot{x} + k_y y + k_x x &= f_y, \end{aligned} \quad (3.6)$$

where d_{xx} is the X -axis damping coefficient, d_{yy} is the Y -axis damping coefficient, d_{xy} is a damping cross-coupling coefficient, k_{xx} and k_{yy} are normalized by a mass resonator rigidity along the X and Y axes, respectively, k_{xy} are rigidity cross-coupling coefficient. It is supposed that $d_{xy}=d_{yx}$ and $k_{xy}=k_{yx}$.

The demodulated slow variables C_x, S_x, C_y, S_y can be transformed into pendulum variables a, q, ϕ' , and θ as follows [16]:

$$\begin{aligned} a &= \sqrt{\frac{1}{2}(E + \sqrt{E^2 - q^2})}; & q &= \sqrt{\frac{1}{2}(E - \sqrt{E^2 - q^2})}; \\ E &= C_x^2 + S_x^2 + C_y^2 + S_y^2; & q &= 2(C_x S_y - C_y S_x); \\ \theta &= \frac{1}{2} a \frac{2(C_x C_y + S_x S_y)}{C_x^2 + S_x^2 - C_y^2 - S_y^2}; & \phi' &= \frac{1}{2} a \frac{2(C_x S_x + C_y S_y)}{C_x^2 - S_x^2 + C_y^2 - S_y^2}; \end{aligned} \quad (3.7)$$

Equations (3.6) for fast variables can be rewritten for pendulum variables for any arbitrary standing wave angle θ and for $q \ll E, \delta\phi = \phi - \phi' \ll 1$, as follows [16]:

$$\begin{aligned} \dot{E} &\approx -\left[\frac{2}{\tau} + \Delta \left(\frac{1}{\tau}\right) \cos 2(\theta - \theta_\tau)\right] E - \frac{\sqrt{E}}{\omega} F_E; \\ \dot{q} &\approx -\frac{2}{\tau} q - \Delta \omega \cos 2(\theta - \theta_\omega) E + \frac{\sqrt{E}}{\omega} F_q; \\ \dot{\theta} &\approx -k\Omega - \frac{1}{2} \Delta \left(\frac{1}{\tau}\right) \sin 2(\theta - \theta_\tau) + \frac{q}{2E} \Delta \omega \cos 2(\theta - \theta_\omega) - \frac{1}{2\omega\sqrt{E}} F_\theta; \\ \delta\dot{\phi} &\approx \dot{\phi} + \frac{1}{2} \Delta \omega \cos 2(\theta - \theta_\omega) + \frac{q}{2E} \Delta \left(\frac{1}{\tau}\right) \sin 2(\theta - \theta_\tau) + \frac{1}{2\omega\sqrt{E}} F_\phi, \end{aligned} \quad (3.8)$$

where F_E, F_q, F_θ , and F_ϕ are control forces that should realize the rate-integrating operation.

The third equation of determines the useful signal proportional to angle rate Ω and measurement errors. As a rule, q (quadrature signal) is close to zero because

there is a control loop to compensate for the quadrature error. Thus, we can neglect the third term in the third equation of the system (3.8).

For the rate-integrating mode of operation force $F_r=0$, and a standing wave angular position changes versus time. In this case, the angle θ is determined to be:

$$\theta \approx -k \int_0^t \Omega dt - \frac{1}{2} \Delta \left(\frac{1}{\tau} \right) \int_0^t \sin 2(\theta(t) - \theta_\tau) dt \quad (3.9)$$

The second term in (3.9) is a whole angle measurement error. This equation reveals the periodic nature of the angle-dependent error.

For constant angle rate Ω , whole angle measurement error $\Delta\theta$ is:

$$\begin{aligned} \Delta\theta(t) \approx -\frac{1}{2} \Delta \left(\frac{1}{\tau} \right) \int_0^t \sin 2(k\Omega t - \theta_\tau) dt = \\ \frac{1}{4k\Omega} \Delta \left(\frac{1}{\tau} \right) \cos(2k\Omega t - \theta_\tau). \end{aligned} \quad (3.10)$$

As can be seen from (3.10) the more the angle rate, the less the amplitude of the whole angle measurement error.

3.2. The angle error determination, approximation and correction

To determine angle error of the rate-integrating CVG, we, first, perform measurements of angle when the gyro rotates with a constant angle rate. We use rate-integrating gyro with cylindrical metallic resonator produced in Ukraine.

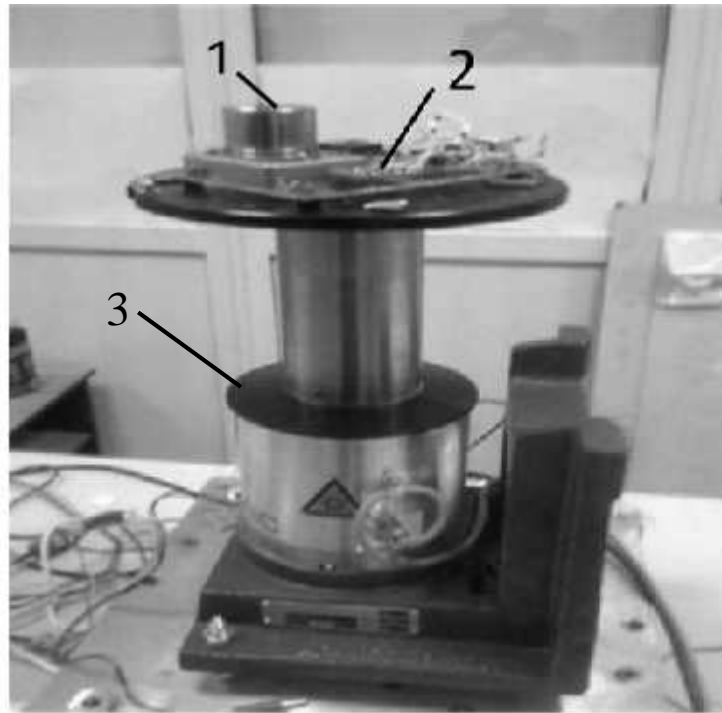


Fig. 3.1. Experimental set-up to measure angle of rotation with metallic resonator CVG

1 – sensing element, 2 – electronic units, 3 – rotating table.

The algorithm of action is represented on the Fig. 3.1:

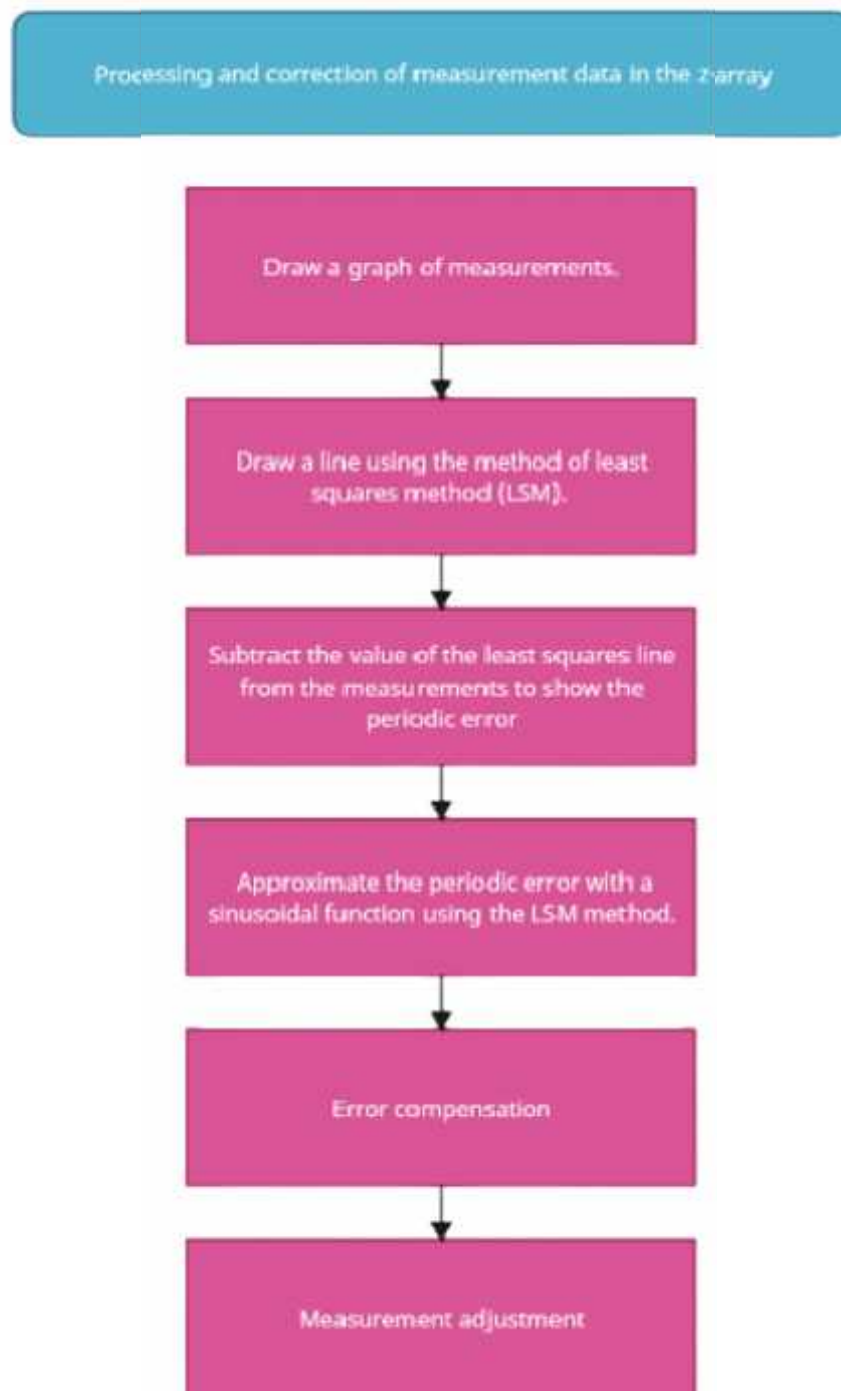


Figure 3.1 - Diagram of processing and correction of measurement data in z-array

The result of the gyroscope measurements was written to the z array and shown in Fig. 3.2:

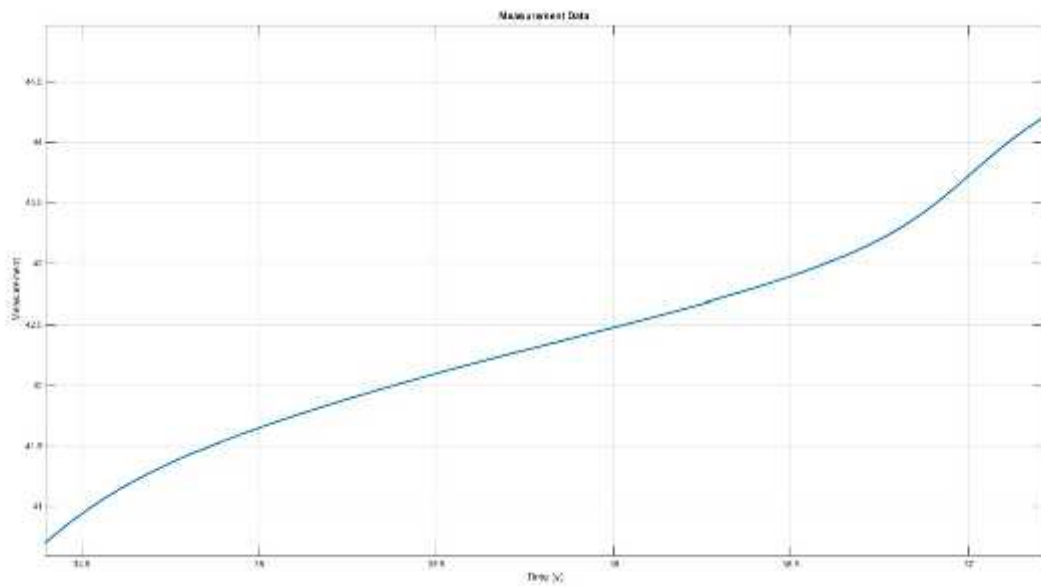


Figure 3.2 - Measured data

After that, we conduct a straight line using the least squares method (LSM), result in a Fig 3.3

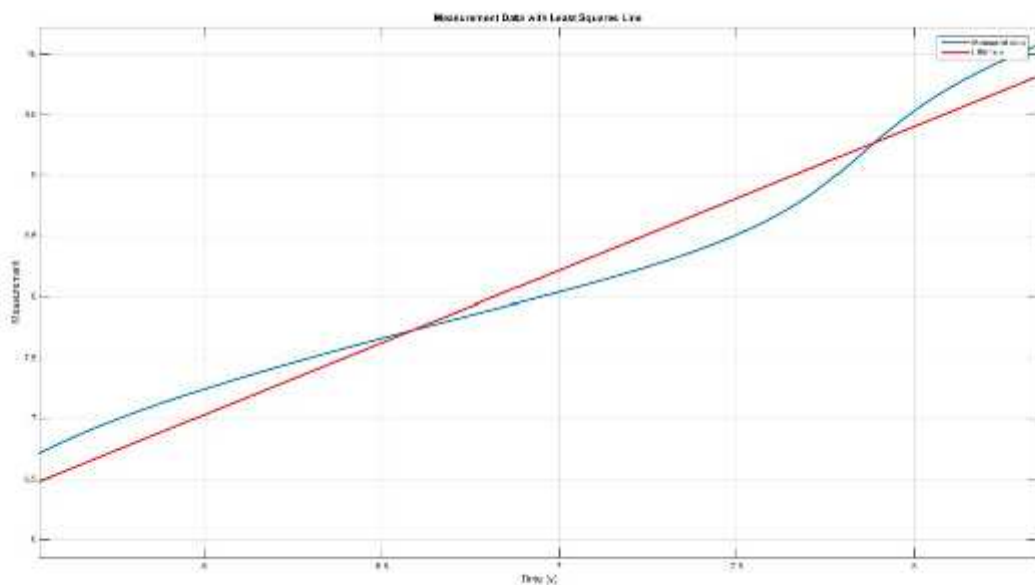


Figure 3.3 - Measured line with Least Square Line

Then subtract the value of the LSM straight line from the measurements. Draw a graph of the difference Fig. 3.4 . The difference shows the periodic error.

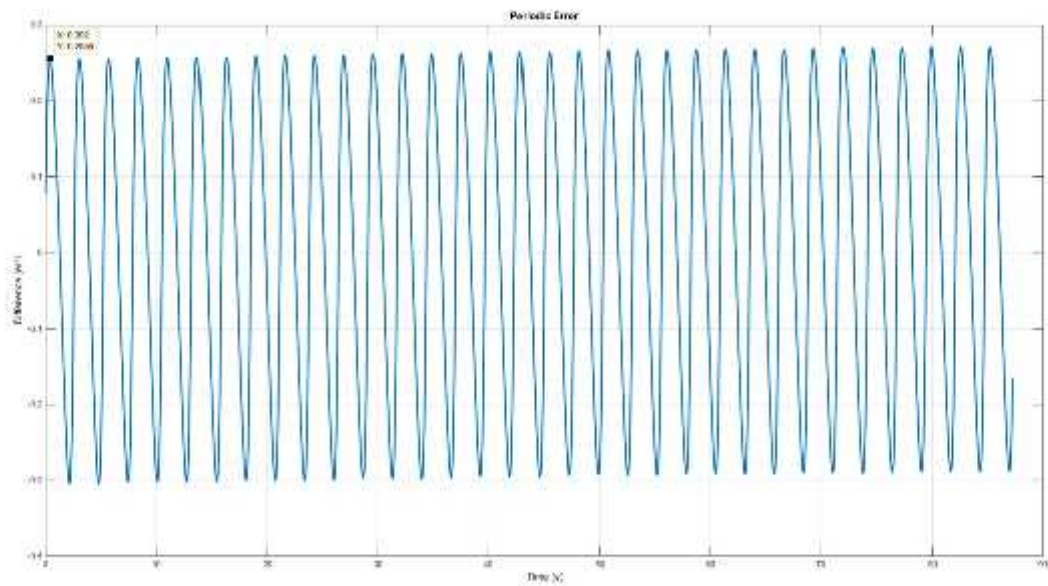


Figure 3.4 - Periodic error

We approximate the periodic error by the sinusoidal function $y_i = A \sin(i\Delta t + \varphi)$ by the method of the LSM (Fig. 3.5).

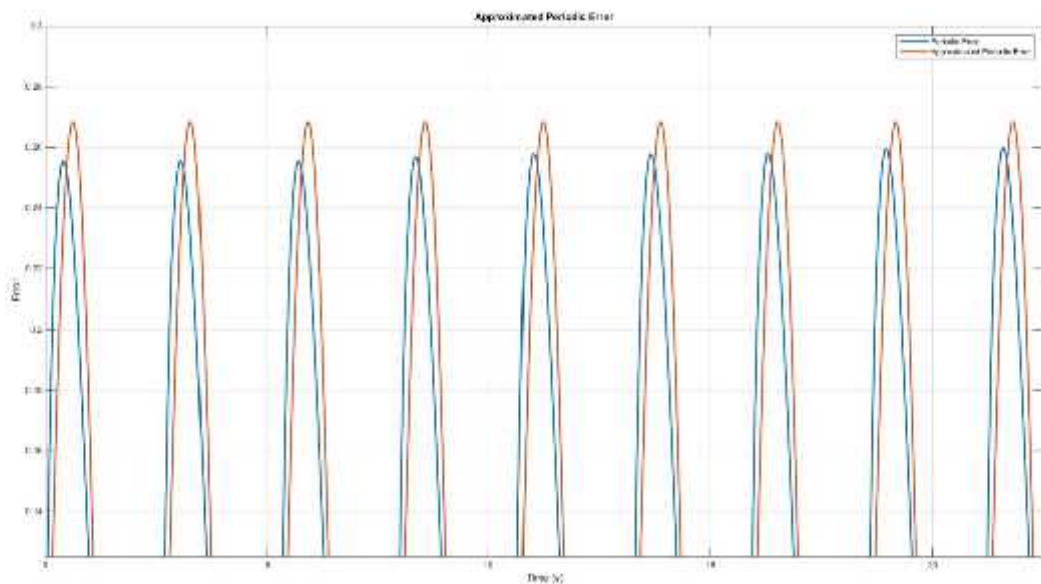


Figure 3.5 - Approximation of periodic error sinusoidal function with the help of LSM method

Subtract the value of the sinusoidal function y_i from the periodic error. This operation is called error compensation. Determine the amplitude of the residual error or its MSE. Find the ratio of the periodic error amplitude to the error compensation amplitude (or MSE). Draw a graph of compensated error.

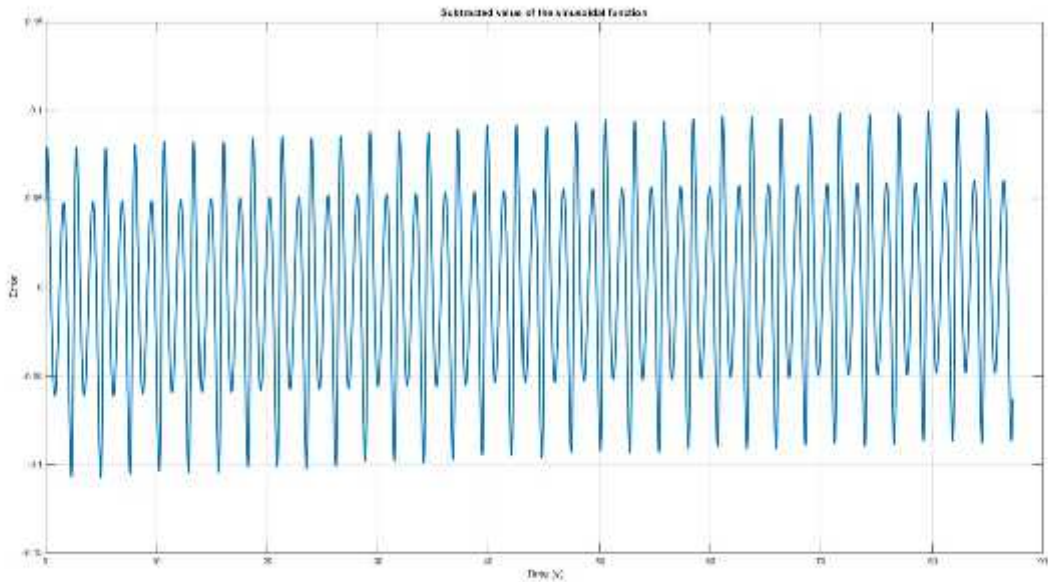


Figure 3.6 - Compensated error

Relation between Periodic error and Compensated is 3.7902. It means, that the measurement accuracy has dropped after error compensation in 3.7 times

Then we draw a z-y graph. This subtraction operation is called a measurement adjustment or correction. Graph represents how changes the graph after error correction

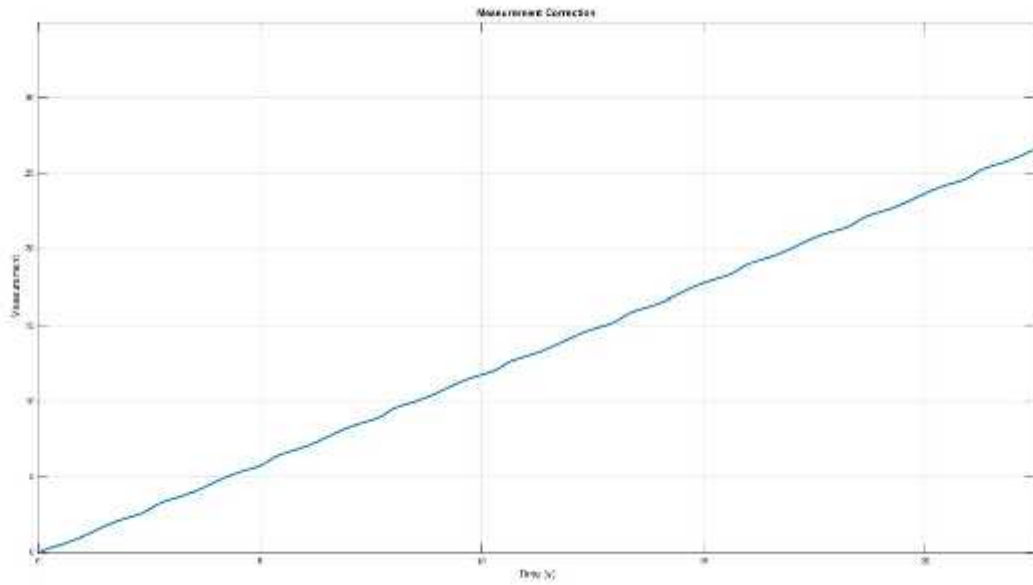


Figure 3.7 - Measurement adjustment

Conclusion

1. The basic error of the vibratory gyroscopes in rate-integrating mode of operation is a periodic bias change due to resonator manufacturing imperfections.
2. The amplitude of this periodic error reduces versus angle rate increasing. Therefore, it expedient to measure rotation angle when angle rate is high.
3. The periodic error component can be corrected by building its model using experimental data.
4. This work shows that using the periodic error correction angle measurement accuracy can be increased by 3.7 time.

References

1. Turner, G. History of Gyroscopes. 2004. Available online: <http://www.gyroscopes.org/history.asp> (accessed on 1 August 2022).
2. Tazartes, D. (Ed.) An historical perspective on inertial navigation systems. In Proceedings of the 2014 International Symposium on Inertial Sensors and Systems (ISISS), Laguna Beach, CA, USA, 25–26 February 2014; IEEE: Piscataway, NJ, USA, 2014. [[Google Scholar](#)]
3. Bergh, R.; Lefevre, H.; Shaw, H. An overview of fiber-optic gyroscopes. *J. Lightwave Technol.* 1984, 2, 91–107. [[Google Scholar](#)] [[CrossRef](#)]
4. Seeger, J.; Lim, M.; Nasiri, S. (Eds.) *Development of High-Performance High-Volume Consumer MEMS Gyroscopes*; Solid-State Sensors, Actuators, and Microsystems Workshop: Hilton Head Island, SC, USA, 2010. [[Google Scholar](#)]
5. Mohammed, Z.; Gill, W.; Rasras, M. Modelling optimization and characterization of inertial sensors. In *Nanoscale Semiconductor Devices, MEMS, and Sensors: Outlook and Challenges*; Springer: Berlin/Heidelberg, Germany, 2017. [[Google Scholar](#)]
6. De Groote, F.; Vandevyvere, S.; Vanhevel, F.; Orban de Xivry, J.-J. Validation of a smartphone embedded inertial measurement unit for measuring postural stability in older adults. *Gait Posture* 2021, 84, 17–23. [[Google Scholar](#)] [[CrossRef](#)] [[PubMed](#)]
7. Mohammed, Z.; Gill, W.A.; Rasras, M.J.I.S.L. Double-comb-finger design to eliminate cross-axis sensitivity in a dual-axis accelerometer. *IEEE Sens. Lett.* 2017, 1, 1–4. [[Google Scholar](#)] [[CrossRef](#)]
8. Ren, D.; Yan, M.; You, Z.J.T.; Technologies, M. Principle and research progress of resonant MEMS magnetometer. *Transducer Microsyst. Technol.* 2007, 26, 10–12. [[Google Scholar](#)]

9. Wendel, J.; Meister, O.; Schlaile, C.; Trommer, G.F. An integrated GPS/MEMS-IMU navigation system for an autonomous helicopter. *Aerosp. Sci. Technol.* 2006, *10*, 527–533. [[Google Scholar](#)] [[CrossRef](#)]
10. Gaura, E.; Newman, R. *Smart MEMS and Sensor Systems*; World Scientific: Singapore, 2006. [[Google Scholar](#)] [[CrossRef](#)]
11. Korvink, J.; Paul, O. *MEMS: A Practical Guide of Design, Analysis, and Applications*; Springer Science & Business Media: Berlin/Heidelberg, Germany, 2010. [[Google Scholar](#)]
12. Younis, M.I. *MEMS Linear and Nonlinear Statics and Dynamics*; Springer Science & Business Media: Berlin/Heidelberg, Germany, 2011. [[Google Scholar](#)]
13. Acar, C.; Shkel, A. *MEMS Vibratory Gyroscopes: Structural Approaches to Improve Robustness*; Springer Science & Business Media: Berlin/Heidelberg, Germany, 2008. [[Google Scholar](#)]
14. Passaro, V.M.N.; Cuccovillo, A.; Vaiani, L.; De Carlo, M.; Campanella, C.E. Gyroscope Technology and Applications: A Review in the Industrial Perspective. *Sensors* **2017**, *17*, 2284. [[Google Scholar](#)] [[CrossRef](#)] [[PubMed](#)]
15. Liu, K.; Zhang, W.; Chen, W.; Li, K.; Dai, F.; Cui, F.; Wu, X.; Ma, G.; Xiao, Q. The development of micro-gyroscope technology. *J. Micromechanics Microeng.* **2009**, *19*, 113001. [[Google Scholar](#)] [[CrossRef](#)]
16. Pistorio, F.; Saleem, M.M.; Somà, A. A Dual-Mass Resonant MEMS Gyroscope Design with Electrostatic Tuning for Frequency Mismatch Compensation. *Appl. Sci.* **2021**, *11*, 1129. [[Google Scholar](#)] [[CrossRef](#)]
17. Nguyen, N.M.; Chang, C.-Y.; Pillai, G.; Li, S.-S. Design of piezoelectric MEMS bulk acoustic wave mode-matched gyroscopes based on support transducer. In Proceedings of the 2021 IEEE 34th International Conference on Micro Electro Mechanical Systems (MEMS), Gainesville, FL, USA, 25–29 January 2021. [[Google Scholar](#)]

18. Iga, Y.; Kanda, K.; Fujita, T.; Higuchi, K.; Maenaka, K. A design and fabrication of mems gyroscope using PZT thin films. In Proceedings of the 2010 World Automation Congress, Kobe, Japan, 19–23 September 2010. [[Google Scholar](#)]
19. Yeh, C.; Tsai, J.; Shieh, R.; Tseng, F.; Li, C.; Su, Y. A vertically supported ring-type mems gyroscope utilizing electromagnetic actuation and sensing. In Proceedings of the 2008 IEEE International Conference on Electron Devices and Solid-State Circuits, Hong Kong, China, 8–10 December 2008. [[Google Scholar](#)]
20. Saqib, M.; Mubasher Saleem, M.; Mazhar, N.; Awan, S.U.; Shahbaz Khan, U. Design and analysis of a high-gain and robust mul-ti-DOF electro-thermally actuated MEMS gyroscope. *Micromachines* **2018**, *9*, 577. [[Google Scholar](#)] [[CrossRef](#)] [[PubMed](#)]
21. Senkal, D.; Efimovskaya, A.; Shkel, A.M. Minimal realization of dynamically balanced lumped mass WA gyroscope: Dual foucault pendulum. In Proceedings of the 2015 IEEE International Symposium on Inertial Sensors and Systems (ISISS), Hapuna Beach, HI, USA, 23–26 March 2015. [[Google Scholar](#)]
22. Zhanshe, G.; Fucheng, C.; Boyu, L.; Le, C.; Chao, L.; Ke, S. Research development of silicon MEMS gyroscopes: A review. *Microsyst. Technol.* **2015**, *21*, 2053–2066. [[Google Scholar](#)] [[CrossRef](#)]
23. Armenise, M.N.; Ciminelli, C.; Dell’Olio, F.; Passaro, V.M. *Advances in Gyroscope Technologies*; Springer Science & Business Media: Berlin/Heidelberg, Germany, 2010. [[Google Scholar](#)]
24. Boxenhorn, B.; Greiff, P. A vibratory micromechanical gyroscope. *Guid. Navig. Control. Conf.* **1988**. [[Google Scholar](#)] [[CrossRef](#)]
25. Greiff, P.; Boxenhorn, B.; King, T.; Niles, L. Silicon monolithic micromechanical gyroscope. In Proceedings of the TRANSDUCERS’91: 1991 International Conference on Solid-State Sensors and Actuators Digest of Technical Papers, San Francisco, CA, USA, 24–27 June 1991. [[Google Scholar](#)]

26. Greiff, P.; Antkowiak, B.; Campbell, J.; Petrovich, A. Vibrating wheel micromechanical gyro. In Proceedings of the Position, Location and Navigation Symposium-PLANS'96, Atlanta, GA, USA, 22–25 April 1996. [[Google Scholar](#)]
27. Bernstein, J.; Cho, S.; King, A.; Kourepenis, A.; Maciel, P.; Weinberg, M. A micromachined comb-drive tuning fork rate gyroscope. In Proceedings of the IEEE Micro Electro Mechanical Systems, Fort Lauderdale, FL, USA, 10 February 1993. [[Google Scholar](#)]
28. Geiger, W.; Folkmer, B.; Merz, J.; Sandmaier, H.; Lang, W. A new silicon rate gyroscope. *Sens. Actuators A Phys.* **1999**, *73*, 45–51. [[Google Scholar](#)] [[CrossRef](#)]
29. Maenaka, K.; Ioku, S.; Sawai, N.; Fujita, T.; Takayama, Y. Design, fabrication and operation of MEMS gimbal gyroscope. *Sens. Actuators A Phys.* **2005**, *121*, 6–15. [[Google Scholar](#)] [[CrossRef](#)]
30. Jain, A.; Shekhar, C.; Gopal, R. Fabrication of two-gimbal Ni–Fe torsional micro-gyroscope by SU-8 based UV-LIGA process. *Microsyst. Technol.* **2014**, *21*, 1479–1487. [[Google Scholar](#)] [[CrossRef](#)]
31. Lee, J.S.; An, B.H.; Mansouri, M.; Al Yassi, H.; Taha, I.; Gill, W.A.; Choi, D.S. MEMS vibrating wheel on gimbal gyroscope with high scale factor. *Microsyst. Technol.* **2019**, *25*, 4645–4650. [[Google Scholar](#)] [[CrossRef](#)]
32. Van Vu, T.; Tran, D.Q.; Chu, T.D. Matching mechanical response for a MEMS vibratory tuning fork gyroscope. *Microsyst. Technol.* **2020**, *26*, 3865–3874. [[Google Scholar](#)] [[CrossRef](#)]
33. Dong, X.; Huang, Q.; Yang, S.; Huang, Y.; En, Y. Model and experiment of scale factor acceleration sensitivity of MEMS gyroscope in high acceleration environment. *Microsyst. Technol.* **2018**, *25*, 3097–3103. [[Google Scholar](#)] [[CrossRef](#)]
34. Che, L.; Xiong, B.; Li, Y.; Wang, Y. A novel electrostatic-driven tuning fork micromachined gyroscope with a bar structure operating at atmospheric pressure. *J. Micromech. Microeng.* **2009**, *20*, 015025. [[Google Scholar](#)] [[CrossRef](#)]

35. Sharma, A.; Zaman, F.; Amini, B.; Ayazi, F. A high-Q in-plane SOI tuning fork gyroscope. In Proceedings of the SENSORS, Vienna, Austria, 24–27 October 2004; pp. 467–470. [[Google Scholar](#)] [[CrossRef](#)]
36. Nguyen, M.N.; Ha, N.S.; Nguyen, L.Q.; Chu, H.M.; Vu, H.N. Z-axis micromachined tuning fork gyroscope with low air damping. *Micromachines* **2017**, *8*, 42. [[Google Scholar](#)] [[CrossRef](#)]
37. Guan, Y.; Gao, S.; Jin, L.; Cao, L. Design and vibration sensitivity of a MEMS tuning fork gyroscope with anchored coupling mechanism. *Microsyst. Technol.* **2015**, *22*, 247–254. [[Google Scholar](#)] [[CrossRef](#)]
38. Guan, Y.; Gao, S.; Liu, H.; Jin, L.; Niu, S. Design and Vibration Sensitivity Analysis of a MEMS Tuning Fork Gyroscope with an Anchored Diamond Coupling Mechanism. *Sensors* **2016**, *16*, 468. [[Google Scholar](#)] [[CrossRef](#)]
39. Trusov, A.A.; Prikhodko, I.P.; Zotov, S.A.; Schofield, A.R.; Shkel, A.M. Ultra-high Q silicon gyroscopes with interchangeable rate and whole angle modes of operation. In Proceedings of the SENSORS, Waikoloa, HI, USA, 1–4 November 2010; pp. 864–867. [[Google Scholar](#)] [[CrossRef](#)]
40. Xia, D.; Yu, C.; Kong, L. The Development of Micromachined Gyroscope Structure and Circuitry Technology. *Sensors* **2014**, *14*, 1394–1473. [[Google Scholar](#)] [[CrossRef](#)]
41. Putty, M.W.; Eddy, D.S. Microstructure for Vibratory Gyroscope. U.S. Patent 5,450,751, 19 September 1995. [[Google Scholar](#)]
42. Ayazi, F.; Najafi, K. Design and fabrication of high-performance polysilicon vibrating ring gyroscope. In Proceedings of the IEEE Eleventh Annual International Workshop on Micro Electro Mechanical Systems An Investigation of Micro Structures, Sensors, Actuators, Machines and Systems, Heidelberg, Germany, 25–29 January 1998. [[Google Scholar](#)]
43. Ayazi, F.; Najafi, K. A HARPSS polysilicon vibrating ring gyroscope. *J. Microelectromech. Syst.* **2001**, *10*, 169–179. [[Google Scholar](#)] [[CrossRef](#)]

44. Ayazi, F.; Chen, H.; Kocer, F.; He, G.; Najafi, K. A High Aspect-Ratio Polysilicon Vibrating Ring Gyroscope. In Proceedings of the Solid-State Sensor Actuator Workshop, Hilton Head Island, SC, USA, 4–8 June 2000; Volume 10, pp. 4–8. [[Google Scholar](#)] [[CrossRef](#)]
45. Guohong, H.; Najafi, K. A Single-Crystal Silicon Vibrating Ring Gyroscope. In Proceedings of the Technical Digest MEMS 2002 IEEE International Conference Fifteenth IEEE International Conference on Micro Electro Mechanical Systems, Las Vegas, NV, USA, 24 January 2002. [[Google Scholar](#)]
46. Kou, Z.; Liu, J.; Cao, H.; Shi, Y.; Ren, J.; Zhang, Y. A novel MEMS S-springs vibrating ring gyroscope with atmosphere package. *AIP Adv.* **2017**, *7*, 125301. [[Google Scholar](#)] [[CrossRef](#)]
47. Kou, Z.; Cui, X.; Cao, H.; Li, B. Analysis and Study of a MEMS Vibrating Ring Gyroscope with High Sensitivity. In Proceedings of the 2020 IEEE 5th Information Technology and Mechatronics Engineering Conference (ITOEC), Chongqing, China, 12–14 June 2020. [[Google Scholar](#)]
48. Syed, W.U.; An, B.H.; Gill, W.A.; Saeed, N.; Al-Shaibah, M.S.; Al Dahmani, S.; Choi, D.S.; Elfadel, I.A.M. Sensor Design Migration: The Case of a VRG. *IEEE Sens. J.* **2019**, *19*, 10336–10346. [[Google Scholar](#)] [[CrossRef](#)]
49. Cao, H.; Liu, Y.; Kou, Z.; Zhang, Y.; Shao, X.; Gao, J.; Huang, K.; Shi, Y.; Tang, J.; Shen, C.; et al. Design, Fabrication and Experiment of Double U-Beam MEMS Vibration Ring Gyroscope. *Micromachines* **2019**, *10*, 186. [[Google Scholar](#)] [[CrossRef](#)] [[PubMed](#)]
50. Gill, W.A.; Ali, D.; An, B.H.; Syed, W.U.; Saeed, N.; Al-Shaibah, M.; Elfadel, I.M.; Al Dahmani, S.; Choi, D.S. MEMS multi-vibrating ring gyroscope for space applications. *Microsyst. Technol.* **2020**, *26*, 2527–2533. [[Google Scholar](#)] [[CrossRef](#)]
51. Liang, F.; Liang, D.-D.; Qian, Y.-J. Dynamical analysis of an improved MEMS ring gyroscope encircled by piezoelectric film. *Int. J. Mech. Sci.* **2020**, *187*, 105915. [[Google Scholar](#)] [[CrossRef](#)]

52. Liang, F.; Liang, D.-D.; Qian, Y.-J. Nonlinear Performance of MEMS Vibratory Ring Gyroscope. *Acta Mech. Solida Sin.* **2020**, *34*, 65–78. [[Google Scholar](#)] [[CrossRef](#)]
53. Fujita, T.; Mizuno, T.; Kenny, R.; Maenaka, K.; Maeda, M. Two-dimensional micromachined gyroscope. In Proceedings of the International Solid State Sensors and Actuators Conference (Transducers' 97), Chicago, IL, USA, 19 June 1997. [[Google Scholar](#)]
54. Juneau, T.; Pisano, A.; Smith, J.H. Dual axis operation of a micromachined rate gyroscope. In Proceedings of the International Solid State Sensors and Actuators Conference (Transducers' 97), Chicago, IL, USA, 19 June 1997. [[Google Scholar](#)]
55. Tang, T.K.; Gutierrez, R.C.; Stell, C.B.; Vorperian, V.; Arakaki, G.A.; Rice, J.T.; Li, W.J.; Chakraborty, I.; Shcheglov, K.; Wilcox, J.Z.; et al. A packaged silicon MEMS vibratory gyroscope for microspacecraft. In Proceedings of the IEEE The Tenth Annual International Workshop on Micro Electro Mechanical Systems An Investigation of Micro Structures, Sensors, Actuators, Machines and Robots, Nagoya, Japan, 26–30 January 1997. [[Google Scholar](#)]
56. Kang, M.-S.; Youn, S.-K.; Cho, Y.-H.; Lee, K.B. Dynamic modeling of a tunable microgyroscope. *Sens. Mater.* **1998**, *10*, 413–424. [[Google Scholar](#)]
57. Prikhodko, I.P.; Zotov, S.A.; Trusov, A.A.; Shkel, A.M. Foucault pendulum on a chip: Angle measuring silicon MEMS gyroscope. In Proceedings of the 2011 IEEE 24th International Conference on Micro Electro Mechanical Systems, Cancun, Mexico, 23–27 January 2011. [[Google Scholar](#)]
58. Prikhodko, I.P.; Zotov, S.A.; Trusov, A.A.; Shkel, A.M. Foucault pendulum on a chip: Rate integrating silicon MEMS gyroscope. *Sens. Actuators A Phys.* **2012**, *177*, 67–78. [[Google Scholar](#)] [[CrossRef](#)]
59. Zotov, S.A.; Trusov, A.A.; Shkel, A.M. High-Range Angular Rate Sensor Based on Mechanical Frequency Modulation. *J. Microelectromech. Syst.* **2012**, *21*, 398–405. [[Google Scholar](#)] [[CrossRef](#)]

60. Minotti, P.; Dellea, S.; Mussi, G.; Bonfanti, A.; Facchinetti, S.; Tocchio, A.; Zega, V.; Comi, C.; Lacaita, A.L.; Langfelder, G. High Scale-Factor Stability Frequency-Modulated MEMS Gyroscope: 3-Axis Sensor and Integrated Electronics Design. *IEEE Trans. Ind. Electron.* **2017**, *65*, 5040–5050. [[Google Scholar](#)] [[CrossRef](#)]
61. D. D. Lynch “Coriolis Vibratory Gyroscope, IEEE Standard Specification Format Guide and Test Procedure for Coriolis Vibratory Gyros”// IEEE std.1431TM, Annex B, pp. 56-66, Dec. 2004.
62. J.A. Gregory “Characterization Control and Compensation of MEMS Rate- and Rate-Integrating Gyroscopes”// Ph.D. Dissertation, Michigan University, P. 198, 2012.
63. J. Y. Cho “High-Performance Micromachined Vibratory Rate- And Rate- Integrating Gyroscopes”// Ph.D. Dissertation, Michigan University, P. 293, 2012.
64. Zh. Su, N. Liu, Q. Li, et al. “Research on the Signal Process of a Bell-Shaped Vibratory Angular Rate Gyro”// *Sensors*, *14*, 5254-5277, 2014; doi: 10.3390/s140305254.
65. B. Gallacher, Zh. Hu, S. Bowles “Full control and compensation scheme for a rate-integrating MEMS gyroscope”// 13th Int. Conf. on Dynamical Systems – Theory and Applications, Lodz, Poland, paper id: ENG267, Dec. 7–10, 2015.
66. J-K. Woo, J. Y. Cho, Ch. Boyd, Kh. Najafi “Whole-Angle-Mode Micromachined Fused-Silica Birdbath Resonator Gyroscope (Wa-Brg)”// IEEE MEMS Conf., San Francisco, CA, USA, January 26–30, 2014.
67. D.D. Lynch, A. Matthews “Dual Mode Hemispherical Resonator Gyro Operating Characteristics”// 3-rd S. Petersburg Int. Conf. on Integrated Navigation Systems, part 1, pp. 37–44, May 1996.

68. V.V. Chikovani, E.O. Umakhanov, P.I. Marusyk “The compensated differential CVG”// Gyro Technology Symposium, Germany, Karlsruhe university, pp. 31-38, 16-17 Sept. 2008.
69. V.V. Chikovani “Method of an angle rate measurement by Coriolis vibratory gyroscope”// Ukr.Patent # 95709, Int.cl.G01 C 19/02. Publ. 25.08.2011, Bul.16/2011 (in Ukrainian).
70. V.V. Chikovani, O. A. Sushchenko “Differential mode of operation for ring-like resonator CVG”// IEEE Proc. Intern. Conf. on Electronics and Nanotechnology, Kyiv, Ukraine, 15–18 April 2014, pp. 451–455.
71. V. V. Chikovani, O. A. Sushchenko, H. V. Tsiрук “External Disturbances Rejection by Differential Single-Mass Vibratory Gyroscope”// Acta Polytechnica Hungarica, 2017, vol. 14, # 3, pp. 251-270.
72. V.V. Chikovani, H.V. Tsiрук “Effective Rejection of Acoustic and Magnetic Field’s Disturbances by Single-Mass Differential Vibratory Gyroscope”// Military-technical digest, National Academy of Land Forces of Ukraine named after P. Sagaidachny, Lviv, #16, 2017, pp. 31-37. (Viyskovo-Tekhnichnyi zbirnik, Natsionalna Academia Sukhoputnykh Viysk im. P. Sagaidachnyi). DOI: <https://doi.org/10.33577/2312-4458.16.2017.31-37>.
73. A. A. Trusov, I.P. Prikhodko, D.M. Rozelle at al. “1 ppm Precision Self-Calibration of Scale Factor in MEMS Coriolis Vibratory Gyroscopes”// Transducers 2013, Barcelona, SPAIN, 16-20 June 2013, pp. 2531-2534.
74. V.A. Matveev, B.S. Lunin, M.A. Basarab “Navigation Systems Based on Solid-State Wave Gyroscopes”// M., Fizmatlit, 2008, P. 239.
75. J. Y. Cho “High-Performance Micromachined Vibratory Rate- and Rate-Integrating Gyroscopes”// Ph.D. Dissert., USA, Michigan University, 2012, P. 293.

76. D.D. Lynch “Vibratory Gyro Analysis by the Method of Averaging”// II
S. Petersburg Conf. on Integrated Navigation System, part I, May 24-25, 1995.-
pp. 26-34.

Appendix

Table 1. Summary of the development of the most common MEMS vibrating gyrosopes.

| Design | Institution | Year | Performance Parameters | Remarks |
|--------|--|------|--------------------------|--|
| Gimbal | The Charles Stark Draper Laboratory, USA [31] | 1988 | - | The first novel design of a micromachined gyroscope was established with no rotating elements. The $350\ \mu\text{m} \times 500\ \mu\text{m}$ device structure was constructed with a two-gimbal system. |
| | The Charles Stark Draper Laboratory, USA [33] | 1996 | Sensitivity of 360 deg/h | A vibrating wheel on a gimbal with a given resonant suspended on a Pyrex substrate. The design shows better sensitivity |

| Design | Institution | Year | Performance Parameters | Remarks |
|--------|--|------|-------------------------|---|
| | | | | than the previous designs. |
| | Institute of Micromachining and Information Technology, Germany [35] | 1999 | Sensitivity of 65 deg/h | The design comprised comb drives, comb electrodes, and primary and secondary oscillatory systems. The gyroscope sensitivity increased with the new innovative design. |
| | University of Hyogo, Japan [36] | 2005 | - | The gyroscope consisted of a two-gimbal system that can operate at atmospheric pressure. |
| | Khalifa University of Science and Technology, UAE | 2019 | - | Several shapes were demonstrated for the MEMS |

| Design | Institution | Year | Performance Parameters | Remarks |
|-------------|---|------|---|---|
| | [38] | | | gimbal gyroscope. A hexagonal structure provides the lowest linear error with a good scale factor. |
| Tuning Fork | The Charles Stark Draper Laboratory, USA [34] | 1993 | Sensitivity of 100 deg/h | Reactive ion-etching fabrication technique used with polysilicon material. |
| | Georgia Institute of Technology Atlanta, Georgia, USA [42] | 2004 | High quality factors of 81,000 for driving and 64,000 for sensing frequency | High-resolution single-crystal silicon on insulator gyroscope developed with higher sensitivity and higher quality factors. |
| | Shanghai Institute of Microsystem and Information Technology, | 2009 | Mismatch of 0.12 kHz with quality factors of 804 and 789 for driving and | Deep reactive ion-etching fabrication technique used for this gyroscope that |

| Design | Institution | Year | Performance Parameters | Remarks |
|--------|--|------|---|--|
| | China [41] | | sensing frequencies, respectively | can operate at atmospheric pressure. |
| | Beijing Institute of Technology, Beijing, China [44] | 2016 | - | Developed a levered system for anchored coupling that increased the in-phase sensing frequency by 50%. |
| | Hanoi University of Science and Technology, Vietnam [43] | 2017 | Sensitivity of 11.56 mV/deg/s at atmospheric pressure | The proposed z-axis gyroscope has a freestanding structure that lowers the air damping. |
| | National University of Defense Technology, China [68] | 2019 | Bias instability of 0.59 deg/h and angle random walk of 0.04 deg/h— h | A polygon shape vibration beam gyroscope with more than 100 Hz bandwidth in a scale ± 200 deg/s |
| | Chinese Academy of Sciences, China | 2021 | Bias instability of 9.27 deg/h and | A gyroscope fabricated with 3D |

| Design | Institution | Year | Performance Parameters | Remarks |
|----------------|---|------|--|--|
| | [69] | | angle random walk 0.923 deg/h— h | wafer level packaging, driving quality factor, and sensing quality factor recorded at roughly 52,000 and 49,300, respectively. |
| | Si-Ware Systems, Egypt [70] | 2022 | Bias instability of 5.5 deg/h and angle random walk 0.2 deg/h— h | Roll-pitch MEMS tuning fork gyroscope developed with in-plane drive mode |
| Vibrating Ring | General Motors Corporation, Detroit, Michigan, USA [48] | 1995 | - | A vibrating ring structure was invented for a vibrating gyroscope with eight support springs. |
| | University of Michigan, Ann Arbor, USA [49] | 1998 | As low as 0.05 deg/h— h angle random walk | A first polysilicon vibrating ring gyroscope was developed with a |

| Design | Institution | Year | Performance Parameters | Remarks |
|---------------|---|-------------|---|--|
| | | | | 30 to 40 μm thick structure. |
| | University of Michigan, Ann Arbor, USA [52] | 2002 | A quality factor of 12,000 with 132 mV/deg/s | A (111) single-crystal silicon material was adopted for the gyroscope. The ring radius was 1.35 mm with 150 μm of structural layer thickness. |
| | University of California, Davis, USA [71] | 2015 | A quality factor of 80,000 with a resonant frequency of 250 kHz | A disk resonator gyroscope with a diameter of 600 μm was reported that operated at the whole-angle mode operation. |
| | University of California, Irvine, USA [72] | 2015 | A quality factor of 100 k with a stable scale factor of 20 ppm | A toroidal ring gyroscope of 1760 μm diameter fabricated with the epitaxial silicon encapsulation |

| Design | Institution | Year | Performance Parameters | Remarks |
|--------|--|------|---|---|
| | | | | fabrication process. |
| | North University of China, China [53] | 2017 | Zero-bias instability measured 61.2 deg/h | A new S-shaped support spring was demonstrated for the ring gyroscope. |
| | Khalifa University of Science and Technology, UAE [55] | 2019 | - | Two different designs of multi vibrating ring structures were demonstrated to enhance the sensitivity for space applications. |
| | North University of China, China [56] | 2019 | Bias instability measured 8.86 deg/h | Double U-beam support springs were introduced to the vibrating ring gyroscope. A deep reactive ion-etching technology is used for |

| Design | Institution | Year | Performance Parameters | Remarks |
|--------|---|------|--|---|
| | | | | microfabrication. |
| | Yangzhou University, China [58] | 2020 | - | The attachment of piezoelectric film increases the gyroscopic sensitivity with forced oscillation and parametric resonance. |
| | University of Windsor, Canada [73] | 2020 | Simulated resonant frequency of 64.89 kHz and experimental resonant frequency of 64.91 | The rose petal-shaped support springs provided better mode matching between driving and sensing resonant modes. |
| | Beijing Institute of Technology, China [74] | 2020 | - | A hinge frame is used with the ring structure. This new design structure provides high linearity and better mode |

| Design | Institution | Year | Performance Parameters | Remarks |
|------------|--|------|--|---|
| | | | | matching. |
| | Zhejiang University, China [19] | 2021 | Geometric analysis | Anisotropy of (100) single-crystal silicon affected MEMS gyroscopic properties. |
| Multi-axis | Himeji Institute of Technology, Japan [60] | 1997 | Sensitivity measured at 0.1 mV/deg/s | A novel two-dimensional design with four cantilever beams that were placed above the glass substrate. |
| | UC Berkeley, Berkeley, CA, USA [61] | 1997 | Angle random walk recorded 2 deg/h-- h | The gyroscope had a 2 μm thick polysilicon disk of 0.3 mm diameter placed 1.6 μm above the substrate and supported by four beams. |

| Design | Institution | Year | Performance Parameters | Remarks |
|--------|--|------|---|--|
| | Korea Advanced Institute of Science and Technology, Korea [63] | 1998 | - | The gyroscope had a polysilicon structure with two suspended plates that vibrated upon electrostatic actuation by comb plates. |
| | National Tsing Hua University, Taiwan [75] | 2005 | Sensitivities measured in the dual-axis sense modes, 7.4 fF/deg/s and 19.4 fF/deg/s | A novel dual-axis vibratory wheel gyroscope with three test masses can measure the two-axis angular rate independently. |
| | University of California, Irvine, USA [64] | 2011 | Linear response in the excess of ± 450 deg/s and 100 Hz bandwidth. Driving and sensing quality factors measured 1.1 million | A four-mass MEMS vibrating gyroscope with a 2 kHz resonant frequency was developed with high quality factors. |

| Design | Institution | Year | Performance Parameters | Remarks |
|--------|--|------|--|--|
| | University of California, Irvine, USA [66] | 2012 | The quality factors for driving and sensing more than a million were measured in the range from $-40\text{ }^{\circ}\text{C}$ to $100\text{ }^{\circ}\text{C}$ | A four-mass MEMS vibrating gyroscope was developed on the frequency modulation. The frequency-modulated gyroscope showed a great stable response at a different range of temperatures. |
| | University of California, Irvine, USA [76] | 2013 | A 1 ppm precision through self-calibration scale factors with temperature changes of $10\text{ }^{\circ}\text{C}$ | A four-mass self-calibration scale factor gyroscope. |
| | University of California, Irvine, USA [28] | 2015 | 100 k quality factors in driving and sensing modes at 2.7 kHz operating resonant | Rate-integrating MEMS gyroscope with dual-test masses. |

| Design | Institution | Year | Performance Parameters | Remarks |
|--------|---|------|--|---|
| | | | frequency | |
| | Korea University of Technology and Education, South Korea [77] | 2020 | - | A three-axis single-drive gyroscope was developed with a driving frequency of 25.44 kHz. |
| | Southeast University, China [78] | 2020 | Mechanical sensitivity was measured at 1.75 nm/deg/s and the micro coil sensitivity is 41.4 mOe/ μ m | A dual-mass MEMS gyroscope that operates by electromotive force and sensing scheme comprising differential tunneling magnetoresistance. |
| | Department of Mechanical and Aerospace Engineering, Politecnico di Torino, Italy [23] | 2021 | Minimize the cross-coupling between driving and sensing frequency by separate masses for the driving and | A comprehensive FEA was conducted on the dual-mass gyroscope for minimizing the |

| Design | Institution | Year | Performance Parameters | Remarks |
|---------------|--------------------|-------------|-------------------------------|----------------|
| | | | sensing axis | mode mismatch. |

Appendix 2

Matlab code:

```
% 1. Draw a graph of measurements.
f = 500; % Sampling frequency in Hz
t = (0:length(z)-1) / f; % Time vector
figure(1)
plot(t, z,'LineWidth',2);
xlabel('Time (s)');
ylabel('Measurement');
title('Measurement Data');
grid;

% 2. Draw a line using the least squares method (LSM)  $x_i = a \cdot \Delta t \cdot i + b$ ;  $i=1 \dots \text{length}(z)$ .
dt = 1 / f; % Time increment
i = 1:length(z); % Indices vector
A = [dt * i', ones(length(z), 1)]; % Design matrix
z=z(:);
coefficients = lsqr(A,z); % Solve for coefficients using LSQR operator
a = coefficients(1); % Extract coefficient a
b = coefficients(2); % Extract coefficient b
line = a * dt * i + b; % Line values
figure(2)
p = plot(t, z,'LineWidth',2);
hold on; % Keep the previous plot
plot(t, line, 'r','LineWidth',2); % Plot the line in red
hold off; % Release the hold on the plot
xlabel('Time (s)');
```

```

ylabel('Measurement');
title('Measurement Data with Least Squares Line');
legend('Measured data', 'LSM line');
grid;
%3. Subtract the value of the least squares line from the measurements. Draw a graph
of the difference err=z-x.
z_extended = z';
err = z_extended - line; % Calculate the difference (err = z - x)
figure(3)
plot(t, err,'LineWidth',2);
xlabel('Time (s)');
ylabel('Difference (err)');
title('Periodic Error');
grid;
%4. Approximate the periodic error err by the sinusoidal function  $y_i = A \sin(i \cdot \Delta t + \phi)$  by the method of the LSM.
fun = @(x, xdata) x(1)*sin(xdata * x(2)+x(3));
xdata = i*dt;
ydata = err;
x0=[0.2658 2.3763 -0.1484];
x = lsqcurvefit(fun,x0,xdata,ydata);
a = x(1)*sin (xdata * x(2) + x(3));
figure (4)
plot(xdata, ydata, xdata, a,'LineWidth',2);
xlabel('Time (s)');
ylabel('Error');
title('Approximated Periodic Error');
legend('Periodic Error', 'Approximated Periodic Error');
grid;

```

%5. Subtract the value of the sinusoidal function y_i from the error err , $err1 = err - y$.

```
err1 = err - a;
```

```
Relation = std(err)/std(err1)
```

```
figure(5)
```

```
plot(xdata, err1, 'LineWidth', 2);
```

```
xlabel('Time (s)');
```

```
ylabel('Error');
```

```
title('Subtracted value of the sinusoidal function');
```

```
grid;
```

%6. Draw a z-y graph. This subtraction operation is called measurement correction.

```
Difference = z'-a;
```

```
figure(6)
```

```
plot(xdata, Difference, 'LineWidth', 2);
```

```
xlabel('Time (s)');
```

```
ylabel('Measurement');
```

```
title('Measurement Correction');
```

```
grid;
```